
A revised L-band radio-brightness sensitivity to extreme winds under tropical cyclones: The 5 year SMOS-Storm database

Reul Nicolas¹, Chapron Bertrand¹, Zabolotskikh E.², Donlon C.^{3,*}, Quilfen Yves¹, Guimbard Sebastien¹, Piolle Jean-Francois¹

¹ Laboratoire d'Océanographie Physique et Spatial (LOPS), Institut Français de Recherche et d'Exploitation de la MER (IFREMER), Centre Bretagne, ZI de la Pointe du Diable, CS 10070, 29280, Plouzané, France

² Satellite Oceanography Laboratory, Russian State Hydrometeorological University (RSHU), Malookhtinsky prosp. 98, St. Petersburg 195196, Russia

³ European Space Agency, ESTEC, Earth Observation Programme Directorate, Mission Science Division, Keplerlaan 1, 2200 AG Noordwijk, The Netherlands

* Corresponding author : C. Donlon

nreul@ifremer.fr

Abstract :

Five years of SMOS L-band brightness temperature data intercepting a large number of tropical cyclones (TCs) are analyzed. The storm-induced half-power radio-brightness contrast (ΔI) is defined as the difference between the brightness observed at a specific wind force and that for a smooth water surface with the same physical parameters. ΔI can be related to surface wind speed and has been estimated for ~ 300 TCs that intercept with SMOS measurements. ΔI , expressed in a common storm-centric coordinate system, shows that mean brightness contrast monotonically increases with increased storm intensity ranging from ~ 5 K for strong storms to ~ 24 K for the most intense Category 5 TCs. A remarkable feature of the 2D mean ΔI fields and their variability is that maxima are systematically found on the right quadrants of the storms in the storm-centered coordinate frame, consistent with the reported asymmetric structure of the wind and wave fields in hurricanes. These results highlight the strong potential of SMOS measurements to improve monitoring of TC intensification and evolution. An improved empirical geophysical model function (GMF) was derived using a large ensemble of co-located SMOS ΔI , aircraft and H*WIND (a multi-measurement analysis) surface wind speed data. The GMF reveals a quadratic relationship between ΔI and the surface wind speed at a height of 10 m (U10). ECMWF and NCEP analysis products and SMOS derived wind speed estimates are compared to a large ensemble of H*WIND 2D fields. This analysis confirms that the surface wind speed in TCs can effectively be retrieved from SMOS data with an RMS error on the order of 10 kt up to 100 kt. SMOS wind speed products above hurricane force (64 kt) are found to be more accurate than those derived from NWP analyses products that systematically underestimate the surface wind speed in these extreme conditions. Using co-located estimates of rain rate, we show that the L-band radio-brightness

contrasts could be weakly affected by rain or ice-phase clouds and further work is required to refine the GMF in this context.

Highlights

► 5 years of SMOS radiometer L-band data intercepts with tropical cyclones are analyzed. ► The storm-induced brightness contrast ΔI monotonically increases with their intensity. ► In average, the brightest ΔI is found in the right-hand side quadrants of the storms. ► A quadratic relationship relates ΔI and the 10 m height surface wind speed (SWS). ► SWS can be retrieved from SMOS with an RMS error of 5 m/s up to 50 m/s.

57 **1 Introduction**

58

59 The measurement of surface wind speed in Tropical Cyclones (TC) is of primary importance for
60 improving storm tracks and intensity forecasts. Unfortunately, obtaining accurate direct or remote
61 measurements at the sea surface level in the extreme conditions of a TC remains a significant challenge
62 (Ulhorn et al., 2007; Powell, 2010, Knaff et al., 2011). Active remote sensing methods of wind
63 measurement saturate in hurricane force winds (e.g., Donnelly et al., 1999) and suffer heavily from rain
64 contamination in the TC's eye wall and outer rain band regions (Weissman et al., 2002). In recent years
65 microwave radiometry has played an important role through the successful development and application
66 of the Stepped Frequency Microwave Radiometer (SFMR) that is the National Oceanic and Atmospheric
67 Administration (NOAA)'s primary airborne sensor for estimating surface wind speed in hurricanes
68 (Uhlhorn et al., 2007). The SFMR instrument measures the brightness temperature of the ocean surface
69 using six distinct C-band frequencies, including frequencies which permit the measurement, and
70 correction for, both rain and surface wind speed. Unfortunately, the SFMR is limited by aircraft range in
71 the North Atlantic and Eastern Pacific and there is still no equivalent sensor capability flying in space
72 today. Most available active and passive orbiting sensors operating in the low microwave frequency
73 bands show poor surface wind speed retrieval performances above hurricane force, largely because of
74 the difficulty to precisely separate wind from rain effects (Powell, 2010).

75 Promising new approaches are nevertheless currently under development based on different
76 sensor technologies. One of these approaches is based on the new capabilities of the Advanced
77 Microwave Scanning Radiometer 2 (AMSR-2) on board the GCOM-W satellite (Zabolotskikh et al.,
78 2015). The method developed by Zabolotskikh et al. (2015) to retrieve sea surface wind speed and rain
79 in tropical cyclones involves the combination of brightness temperature data acquired at the six C- and
80 X-band channels of AMSR-2. Contrarily to the previous AMSR and AMSR-E sensor series, which only
81 operated a single ~6.9 GHz channel, AMSR-2 is now also equipped with an additional C-band channel
82 at 7.3 GHz designed to mitigate for Radio-Frequency Interference (RFI). Using this new channel help to
83 separate the respective contributions from the wind-induced and rain-induced emissivity signal : this has

84 been efficiently exploited in the multi-frequency algorithm of Zabolotskikh et al. (2015). Other promising
85 approaches for spaceborne remote sensing of high surface wind speeds include the exploitation of active
86 cross-polarization C-band SAR data (see Horstmann et al., 2013), and L-band GPS bistatic scatterometry
87 (Ruf et al., 2013) following the launch of CYGNSS mission scheduled in 2016.

88

89 L-band passive and active measurements from the European Space Agency Soil Moisture and
90 Ocean Salinity (SMOS), the NASA Aquarius-SAC/D and the recently launched Soil Moisture Active
91 Passive (SMAP) missions offer new unique opportunities to complement existing ocean satellite high
92 wind observations in TCs and severe weather. This is because upwelling radiation at 1.4 GHz (L-band)
93 is significantly less affected by rain and atmospheric effects than at higher microwave frequencies (Reul
94 et al., 2012). SMOS provides multi-angular L-band brightness temperature images of the Earth over a
95 ~1000 km swath at about ~43 km nominal resolution. SMAP performs simultaneous measurement of L-
96 band brightness temperature, at spatial resolutions of about 40 km across the entire swath ~1000km wide
97 (Entekhabi et al., 2014). Both missions provide data with global coverage in about 3-days due to their
98 large swath. In the context of TC surface wind speed retrieval, the Aquarius sensor is limited because of
99 the low spatial resolution of the three L-band microwave radiometers (~100 km) and the relatively
100 narrow width of their swaths (~300 km when combining all 3 beams), resulting in a global revisit time
101 of only 7 days. While the combination of passive and active L-band measurements is an emerging and
102 promising approach for surface wind speed retrieval in extreme conditions, in this paper, we shall focus
103 only on the brightness temperature signatures of TCs as observed by the SMOS radiometer between
104 2010-2015.

105 The first demonstration of SMOS L-band passive microwave data could be used to retrieve
106 meaningful surface wind speed in TCs has been provided in (Reul et al., 2012). The L-band microwave
107 brightness temperature contrast of the sea surface, defined as the difference between the brightness
108 temperature observed at surface level at some wind force and the brightness temperature of the smooth
109 water surface with the same physical parameters (temperature and salinity), were evaluated. The induced

110 radio-brightness contrasts observed by SMOS as it intercepted storm Igor, a category 4 hurricane, at
111 several stages of its evolution during 11 to 19 September 2010, were co-located and compared to
112 observed and modelled surface wind speed products. From this dataset, a first Geophysical Model
113 Function (GMF) was proposed to describe the relation between the half power L-band radio-brightness
114 contrast of the ocean with the surface wind speed modulus at a height of 10m (U10). The radio-brightness
115 contrast is defined by:

$$116 \quad \Delta I = \Delta (T_h + T_v) / 2 \quad (1)$$

117 where T_h and T_v are brightness temperature in horizontal and vertical polarization, respectively. ΔI was
118 found to increase quasi-linearly with increasing wind speed with a significant change of sensitivity
119 ($\partial \Delta I / \partial U$) from ~ 0.15 K/(kt) below hurricane force (~ 64 kt) to ~ 0.36 K/(kt) above. The GMF was used
120 to retrieve surface wind speed from SMOS data over independent storm Igor intercepts. The radii of 34,
121 50, 64 knots and of the maximum surface wind speeds (that are used to show the bi-dimensional
122 evolution of the surface wind speed structure), were shown to be consistent with the NOAA/Geophysical
123 Fluid Dynamic Laboratory (GFDL) hurricane model solutions and the H*WIND analyses (Powell et al.,
124 1998) from the Hurricane Research Division (HRD) of the Atlantic Oceanographic and Meteorological
125 Laboratory. The authors concluded that the surface wind speed modulus over ~ 40 km pixels can be
126 retrieved with a root mean square error of ~ 10 kt (~ 5 m/s).

127 Heavy rain and ice clouds in the atmosphere have a potential impact on the L-band radio-
128 brightness contrasts, and sea state effects remain rather uncertain and could also be sources of larger
129 amplitude local errors on the retrieved surface wind speed. These effects were not considered in the GMF
130 of Reul et al. (2012). The effect of rain and the atmosphere on radio emission from the sea surface is
131 certainly weaker at L-band than it is at the higher frequencies (Reul et al., 2012). Atmospheric
132 contributions are dominated by absorption and emission due to oxygen at L-band and can be corrected
133 with negligible errors (Yueh et al., 2001) with respect the magnitude of the wind-induced surface radio-
134 brightness contrasts. The absorption due to rain of upwelling radiations is also two order of magnitude
135 larger at C-band frequencies compared to those at L-band (see Fig2b in Reul et al., 2012). Nevertheless,

136 high wind regions in TC are very often associated with extreme rain rates and the atmosphere around the
137 eye walls is very often associated with high concentration of several hydrometeor species such as cloud
138 water, ice, snow, and graupel (Houze et al., 1976). Small ice particles exist between the eye wall and
139 outer rain bands, and graupel particles are collocated with the radius of maximum tangential wind (Houze
140 et al., 1992). Hurricanes are usually glaciated everywhere above the -5°C level and the stratiform cloud
141 areas are dominated by snowflakes (aggregates) at these levels (Black and Hallett., 1986). The impact on
142 L-band emissions of ice phase clouds, of the concomitant high rain rate around a TC eye wall and rain
143 bands remains largely unknown. In Reul et al. (2012) an attempt to quantitatively evaluate the rain impact
144 at a given wind speed was performed using co-located rain rate measurements from various microwave
145 sensors by classifying the estimated L-band radio-contrasts in both rain-free and rainy conditions during
146 four intercepts of storm Igor. Based on the limited data used and previous radiative transfer simulations,
147 it was concluded that rain has a negligible impact on the L-band brightness temperature at high winds,
148 except in very high-extreme rain rates. In those conditions, the maximum rain impact can induce a wind
149 speed retrieval error of up to $\sim 12\text{kt}$ ($\sim 6\text{ m/s}$). To reduce these effects further requires a better knowledge
150 of the rain and ice impacts over a statistically significant number of storm samples from which a new
151 GMF can be derived.

152 The brightness temperature of the ocean is strongly dependent on the foam coverage due to
153 whitecap and streaks induced by wave breaking and wind tearing of the wave crest (Nordberg et al. 1971,
154 Ross and Cardone 1974, Webster et al. 1976, Holthuijsen et al., 2012) but also on the distribution of foam
155 formation thickness (Newell and Zakharov, 1992; Reul and Chapron, 2003, Anguelova and Gaiser 2012;
156 Golbraikh and Shtemler, 2016). Recent observations from Holthuijsen et al., 2012 suggest that the
157 whitecap coverage is not increasing at hurricane wind force and above to reach a constant value of about
158 4%. The “whitening” of the sea surface observed above 64 kt is therefore dominated by the growth of
159 streak coverage. Whether it is the increasing coverage of these streaks, or the increasing thickness of the
160 whitecaps, or a combination of both that explain the quasi-linear growth of the radio-brightness at L-
161 band remains an open question. Both characteristics can be related to wind speed, but surface wave

162 breaking and streak generation are also strongly dependent on wave growth, wave-wave and wave-
163 current interaction, water depth and the changing (turning) direction of winds. The physics of wave
164 breaking generation processes within hurricanes is complicated by the rapidly turning winds that generate
165 cross-seas and higher sea state in the forward right-hand quadrant of storms in the northern hemisphere
166 (and in the left-hand quadrant for the southern hemisphere). The velocity of forward movement of the
167 storm, the maximum wind velocity, and radius of maximum wind for a given storm as well as the duration
168 of wind action with respect group velocity of waves, are key parameters known to play an important role
169 in determining both the magnitude and spatial distribution of the waves generated within storm quadrants
170 (Young, 2003; MacAfee and Bowyer, 2005, Kudryavtsev et al., 2015). The wave field is thus more
171 asymmetric than the corresponding wind field, mainly due to the “extended fetch” which exists to the
172 right (left in the Southern hemisphere) of a translating hurricane due to relative wind/wave motions. It
173 is worth noting that the effects of wave-current interaction on surface foam formation may also be
174 important for hurricanes in some areas, e.g. in the U.S., due to the strong influence of either the Gulf
175 Stream (Western Atlantic) or the Loop Current (Gulf of Mexico). Yet, the impact on the radio-brightness
176 contrast at L-band of wave and wave breaking development and variability in storm quadrants is still
177 poorly known. Thus, algorithms for wind speed retrieval from L-band microwave radiometry must be
178 developed that are sensitive to these effects using a statistically significant number of storm samples from
179 which a new GMF can be derived.

180 In this paper, we present results of a study conducted to extend the initial work of Reul et al.
181 (2012) and gain further insight into wind, rain, and sea state effects on L-band radio brightness contrasts.
182 We systematically produced L-band SMOS radio-contrasts and high wind speed retrievals and generated
183 a global database of SMOS intercepts with all TC events that developed over the global ocean during the
184 period January 2010 to April 2015. Data and processing are described in the first section. We then show
185 several examples of the SMOS radio-contrast signal and retrieved winds for various representative
186 storms. In part three, we analyse the statistical properties of the L-band brightness temperature contrasts
187 as function of storm sectors and storm intensity to illustrate the capability of L-band passive microwave

188 data to provide a metric for intensity change in TCs. We then validate SMOS retrieved winds based on
189 the first GMF derived by Reul et al., 2012 using different surface wind speed products. The quality of
190 SMOS wind is then assessed and compared to European Center Medium-range Weather Forecasts
191 (ECMWF) and Numerical Centers for Environmental Prediction (NCEP) wind speed products in the
192 range 0-100 kt. Based on these co-located data sets, a refined new GMF function is proposed. Finally,
193 we discuss the limitations and characteristics associated with the new L-band observations (potential
194 effects of rain and sea state and others) and the enhanced storm tracking capability that are now possible
195 using merged SMOS-AMSR2 and SMAP data.

196 **2 Data and Methods**

197 **2.1 SMOS data and processing**

198 SMOS brightness temperature (T_B) images are formed through Fourier synthesis from the cross
199 correlations between simultaneous signals obtained from pairs of antenna elements. For this study, we
200 used the SMOS Level 1B V620 products, generated by the ESA/SMOS Data Processing Ground Segment
201 (DPGS). The SMOS Level-1B (L1B) product is the output of the image reconstruction of the
202 observations and comprises the Fourier component of the T_B in the antenna polarization reference frame.
203 Level-1B corresponds to one temporal measurement, i.e., the whole field of view, one integration time,
204 and is often called a ‘snapshot’. T_B images are then obtained by applying an inverse Fast Fourier
205 Transform (IFFT) to the Level 1B T_B Fourier coefficients using a Blackman spatial filter as described
206 by Anterrieu et al. (2002). The reconstructed T_B product at the top of the atmosphere is geo-located in an
207 equal-area grid system (ISEA 4H9 - Icosahedral Snyder Equal Area projection) with an oversampled
208 spatial resolution of about ~ 15 km. We consider here T_B data reconstructed in the extended field of view
209 (FOV) domain of the antenna for which the swath width is approximately 1200 km (see Font et al., 2010,
210 Figure 6). The actual spatial resolution of the reconstructed T_B data varies within the FOV from ~ 32 km
211 at boresight to about ~ 80 km at the edges of the swath (43 km on average over the field of view). The
212 earth-view incidence angle ranges from nadir to about 60° and the radiometric accuracy from 2.6 K at
213 boresight to about 4–5 K on the swath edges. As the satellite moves, multiple observations of the same

214 pixel at different incidence angles are obtained from successive snapshots. Earth grid point with less than
215 5 multi-angular observations (typically encountered at the extreme border of the swath) are removed.

216 The L-band T_B measured by a downward looking radiometer such as that on board SMOS are
217 significantly influenced by a number of radiation sources (Yueh et al., 2001; Font et al., 2010). The most
218 important sources of L-band brightness over the ocean are: (1) perfectly flat surface emission (with order
219 of magnitude $\sim 100 \pm 4$ K due to Sea Surface Salinity (SSS) and Sea Surface Temperature (SST) variability
220 impact); (2) atmospheric emission (on the order of ~ 5 K including reflected down-welling and upwelling
221 emissions); (3) scattered cosmic background and galactic radiation incident at the surface (order of
222 magnitude ~ 10 K); and (4) excess emission associated with the wind-driven surface roughness and
223 breaking-wave generated foam (order of magnitude $\sim 10 - 30$ K depending on the wind strength). All but
224 one of these contributions can be estimated using data together with the SMOS Level 2 radiative transfer
225 forward model of scene brightness (Zine et al., 2008) to generate individual residual sources ΔT_B of
226 brightness contrast. Using this approach, we removed all but the rough and foam-surface emission
227 contributions from the SMOS measurements. In the SMOS forward model (Zine et al., 2008), the
228 evaluation of atmospheric contributions do not account for potential rain impact, which is hereafter
229 neglected. The resulting data set is then used to reveal the impact of surface roughness and foam changes
230 on the SMOS T_b in TC conditions. Additional geophysical auxiliary data required to evaluate the
231 different forward model contributions are obtained operationally at the SMOS measurement time and
232 location by the DPGS using products from ECMWF.

233 To estimate the flat sea surface emission contribution, we used the ECMWF/OSTIA Sea Surface
234 Temperature daily night time products (Donlon et al. 2012) and we estimated the sea surface salinity
235 (SSS) using SMOS SSS data themselves for the week preceding the passage of the storms. For this study,
236 we used the Centre Aval de Traitement des Données SMOS (CATDS, www.catds.fr) Expertise Center-
237 Ocean Salinity SMOS SSS (IFREMER V02) Level 3 products (Reul and Ifremer CATDS-CECOS Team,
238 2011). Data were first processed to provide a level 3 daily gridded SSS field at a spatial resolution of
239 $0.25^\circ \times 0.25^\circ$ for the complete year. Composite weekly products were then generated for each storm

240 using a 7-day running mean and a 0.5° spatial window. The SSS was further bi-linearly interpolated to
 241 15 km resolution to evaluate the brightness contrast ΔT_B induced by salinity and temperature changes
 242 alone. Reul et al. (2012) estimated that SSS errors on the order of ~ 0.5 practical salinity scale (the accuracy
 243 of weekly CATDS products in the tropics) will translate into maximum wind speed bias of ~ 1 m/s.
 244 Nevertheless, large tropical river plumes (Amazon, Mississippi) can exhibit significant SSS variability on
 245 time scales less than a week (eg. tidal effects, currents, sudden increase in the river discharge): using SSS
 246 fields estimated from preceding weekly data in such high variability areas may be an additional source
 247 of local error on the retrieved wind speed.

248 Polarization mixing (Faraday rotation), due to the electromagnetic wave propagation through the
 249 ionosphere in the presence of the geomagnetic field (Skou and Hoffman-Bang, 2005) is an additional
 250 source of L-band Tb modification as measured from space. It can be either modelled from the knowledge
 251 of the ionospheric Total Electron Content (TEC) and magnetic field or avoided by using the first Stokes
 252 parameter:

$$253 \quad I = T_H + T_V \quad (2)$$

254 which is invariant by rotation. We choose such alternative approach and estimate both the first Stokes
 255 surface roughness and foam-induced Tb residual using:

$$257 \quad \Delta I = \Delta T_H + \Delta T_V \quad (3)$$

259 Finally, to reduce the SMOS instrument instantaneous radiometric noise (that can vary from 2.6
 260 – 5.0 K for a single snapshot measurement as function of the position of the pixel within the swath), we
 261 average the SMOS multi-angular measurements at a given location to estimate an ‘incidence-angle
 262 averaged’ first Stokes brightness temperature residual generated by surface roughness and foam:

$$264 \quad \overline{\Delta I} = \frac{1}{\theta_{max} - \theta_{min}} \int_{\theta_{min}}^{\theta_{max}} \Delta I(\theta) d\theta \quad (4)$$

265

266 where θ is the earth incidence angle and $[\theta_{min}, \theta_{max}] \approx [10^\circ, 60^\circ]$.

267 The different spatial resolution within the SMOS swath (a function of incidence angle) increases the
268 uncertainty in the estimated surface $\overline{\Delta I}$. A weighted average of the ΔI (designed to minimise the
269 contribution from the largest pixels) would potentially reduce errors associated with variable spatial
270 resolution. However, a simple averaging procedure was chosen to systematically and consistently reduce
271 the relatively high instrument instantaneous radiometric noise. The noise-reduction approach through
272 incidence-angle averaging is necessary in the context of SMOS because of the low signal-to-noise ratio
273 for a single angle measurement. The approach is justified by the fact that a small incidence-angle
274 dependence of the foam impact is expected from radiative transfer models of foam emissivity at L-band
275 in the range 0° – 50° (Reul and Chapron, 2003; Camps et al., 2005; Yueh et al., 2010), a characteristic
276 which was confirmed in the observations over hurricane Igor (Reul et al., 2012). In this paper we will
277 consider the half total power:

278

$$279 \quad \frac{\Delta I}{2} = \Delta(T_H + T_V)/2 \quad (5)$$

280

281 and for clarity, we shall drop the overbar notation. Unless specified, ΔI will therefore always refer to the
282 incidence angle-averaged half-power quantity. Surface wind speed modulus is finally retrieved from ΔI
283 data using the bi-linear GMF proposed in Reul et al. 2012, hereafter referred to as GMF1.

284 **2.2 Storm Tracks and Intensity**

285 Tropical cyclone “best track” data (Jarvinen et al. 1984) were obtained from the WMO International Best
286 Track Archive for Climate Stewardship (IBTrACS, Knapp et al. 2010). We used the best track archive
287 dataset version v03r06 available at NOAA National Climatic Data Center
288 (<https://www.ncdc.noaa.gov/ibtracs/>). The database includes 6-hourly storm center track location and
289 maximum one-minute sustained wind speed information. We used the "source" datasets in the Best track
290 data that combines information from the most reliable tropical cyclone data centres. At the time this work

291 was conducted, the IBTrACS tracks database only included few storms in 2014 and none in 2015. For
292 these two years, we completed the storm track database using data from the Joint Typhoon Warning
293 Center (JTWC) and National Hurricane Center (NHC).

294 Best-track data are a subjectively-smoothed representation of a tropical cyclone's location and intensity
295 over its lifetime and generally will not reflect the erratic motion implied by connecting individual center
296 fix positions. In the present work, the position of the storm centre at the time of SMOS acquisition was
297 determined by default using a linear interpolation in time of the best track data. Uncertainties on the
298 estimate of the storm centre location at SMOS acquisition time nevertheless result from the combined
299 errors of the smoothed representation of the best-track data and from the use of a linear time-interpolation
300 method. The NOAA/Hurricane Research division proposes alternative wind center fixes and interpolated
301 tracks using a series of spline curves with varying degrees of curvature (Willoughby and Chelmon,
302 1982). However, such interpolated track data are only available for those North Atlantic and East Pacific
303 hurricanes in which aircraft reconnaissance flights were performed. As we processed a large number of
304 storms in other basins without aircraft data, microwave 85 GHz data from SSMI/IS 15-16-17-18, TMI,
305 WindSAT, AMSR-E and AMSR-2 were used for complementary checks. The latter data are available
306 from the Morphed Integrated Microwave Imagery (MIMIC-TC) database provided by the Cooperative
307 Institute for Meteorological Satellite Studies Space Science (CIMSS). Adjustments were performed if a
308 visual inspection revealed discrepancy between the best tracks interpolated storm-center location, the 85
309 GHz and the SMOS fields (e.g., cases when the centre is very easily detectable on SMOS data by visual
310 inspection but displaced from best track or 85 GHz's estimates). The bearing of the storm center main
311 motion at SMOS acquisition time was also estimated from the time interpolated 6-hourly best-track data.

312 **2.3 Surface wind speed products**

313 SMOS retrieved winds are compared with a set of alternative surface wind speed datasets including
314 Numerical Weather products and retrieved surface winds from either the SFMR operated aboard the

315 NOAA and Air Force aircrafts or H*WIND analyses (Powell et al., 1998). Both data are available from
316 the Hurricane Research Division (HRD) of the Atlantic Oceanographic and Meteorological Laboratory.
317 The SFMR was specifically developed to measure hurricane-force ocean surface winds and is typically
318 mounted on aircraft that makes reconnaissance flights with radial passes through the center of TCs. The
319 SFMR measures the nadir brightness temperatures between 4.5 and 7.2 GHz and the data available are
320 processed with a 10-second running mean to derive surface wind speeds and rain rates using dedicated
321 GMF (Uhlhorn et al., 2007) at a resolution of ~3km. Based on a comparison of SFMR to GPS dropsonde
322 wind speed measurements, an error of approximately 4 m/s in TC winds between 10 and 70 m/s is
323 expected (Uhlhorn et al., 2007).

324 To validate and re-analyse the SMOS GMF, we also used H*WIND two-dimensional surface wind
325 analysis products (Powell et al., 1998). The H*WIND analysis uses a combination of all available surface
326 and near surface wind observations collected over a period of several hours from multiple platforms (i.e.,
327 SFMR wind speeds, GPS dropwindsondes, tail Doppler radar, geostationary operational environmental
328 satellite (GOES) cloud track winds, surface ships and buoy data as well as satellite observations (such as
329 QuikSCAT, WindSat and ASCAT), etc.). The analysis procedure adjusts each data set to a common
330 elevation and exposure and creates a 6 km resolution surface wind field for each TC in a "storm-centric"
331 moving coordinate system. The wind speed represents the one-minute sustained wind velocity at 10-m
332 height reference. These objectively analyzed wind products are used routinely as guidance for operational
333 TC forecast and advisory products, including the determination of wind radii (e.g., radius of maximum
334 wind and at 34, 50, and 64 kt winds) by hurricane forecasters at the National Hurricane Center and the
335 Central Pacific Hurricane Center. The H*WIND accuracy is highly dependent on the quality of the
336 dataset and data coverage used as input. Although it is imperfect, it is the best 2D surface truth currently
337 available. Note that these fields are only freely available now until 2013, post 2013 data will be made
338 available for non-commercial research purposes (M. Powell, pers. Comm.).

339 Prior to making comparisons with SMOS data, all SFMR and H*WIND measurements are
340 adjusted for the time difference between SMOS acquisitions by shifting the movement of the storm centre

341 according to the time difference. This results in adjusted flight tracks such that SFMR and H*WIND
342 measurements have the same location with respect to the centre of the storm at the time of the SMOS
343 acquisition as they actually had when they were recorded. This adjustment does not consider any storm
344 rotation. The storm's movement is derived from the best track information from IBTrACS. We
345 considered all SFMR and H*WIND observations available within ± 12 hours from SMOS data. The two
346 closest H*WIND wind fields in time before and after a SMOS overpass of a given TC available ± 12
347 hours from SMOS were linearly interpolated to the SMOS acquisition time. To assess the performance
348 of SMOS winds, comparisons were performed with both SFMR and H*WIND products kept at their
349 original spatial resolution, respectively 3 and 6 km, but smoothed to match the SMOS average spatial
350 resolution by using a running spatial 2D Gaussian windows (Brinkman and Bodschwinn, 2003) with
351 standard deviation equal to 43 km.

352 Note that Hurricane surface winds are strongly dependent on the averaging time attributed to the
353 wind observations, the roughness of the underlying surface, and height of the wind measurements above
354 the sea surface. The NHC best track maximum sustained surface wind is defined as the maximum one-
355 minute wind observed at a height of 10 m. Here, all the other wind products are also referred to a 10 m
356 height. The H*WIND averaging time is also one minute, so that the SMOS retrieved wind speeds derived
357 using the GMF of Reul et al. (2012) are calibrated based on a one-minute averaging period. However,
358 the SMOS spatial resolution is much coarser and a better approach, more consistent with the spatial
359 resolution of SMOS, is to use the maximum 10-minute wind as used by most of world's operational
360 centers outside of the USA. Therefore, all wind speed value derived based on a 1 minute averaging period
361 were adjusted to a 10-minute standard: 10-minute averaged wind speed are $\sim 7\%$ smaller than 1-minute
362 averages (Harper et al., 2008).

363 The performance of SMOS winds in storms with respect to numerical weather forecast fields from
364 ECMWF and NCEP operational models are assessed using ECMWF 10-m equivalent neutral wind data
365 that are also used as auxiliary information in the SMOS operational SSS Level 2 processor. Six-hourly

366 GFS NCEP wind speed products were also co-located in space and linearly interpolated in time with
367 SMOS acquisition and compared to paired SMOS/H*WIND data.

368 **2.4 Rain data**

369 We use satellite rainfall rate estimates from the CMORPH products (CPC MORPHing technique) that
370 include global precipitation analyses at high spatial (~8km) and temporal resolution (~3 hourly). The
371 approach (Joyce et al., 2004) uses precipitation estimates derived exclusively from low earth orbit
372 satellite microwave observations, and whose features are advected via spatial propagation information
373 that is obtained from geostationary satellite infrared (IR) data. At present NOAA incorporate
374 precipitation estimates derived from the following satellites instruments: DMSP 13, 14 and 15 (SSM/I),
375 NOAA-15, 16, 17 and 18 (AMSU-B), Aqua (AMSR-E), TRMM (TMI) and GPM (DPR and GMI). IR
376 data are used as a means to propagate the microwave-derived precipitation features during periods when
377 microwave data are not available to a given location. Propagation vector matrices are produced by
378 computing spatial lag correlations on successive images of geostationary satellite IR that are then used
379 to propagate the microwave derived precipitation estimates. This process governs the movement of the
380 precipitation features only. At a given location, the shape and intensity of the precipitation features in the
381 intervening half hour periods between microwave scans are determined by performing a time-weighting
382 interpolation between microwave-derived features that have been propagated forward in time from the
383 previous microwave observation and those that have been propagated backward in time from the
384 following microwave scan. NOAA refer to this latter step as "morphing" of the features. CMORPH
385 estimates cover a global belt (-180° W to 180° E) extending from 60° S to 60° N latitude and are available
386 at ftp://ftp.cpc.ncep.noaa.gov/precip/CMORPH_V1.0/RAW/

387 With regard to spatial resolution, although the precipitation estimates are available on a grid with a
388 spacing of 8 km (at the equator), the resolution of the individual satellite-derived estimates is coarser
389 than that - more on the order of 12 x 15 km. The finer "resolution" is obtained via interpolation. Similarly
390 to the wind speed products, we estimated the rain rate on the SMOS 15km resolution grid by averaging

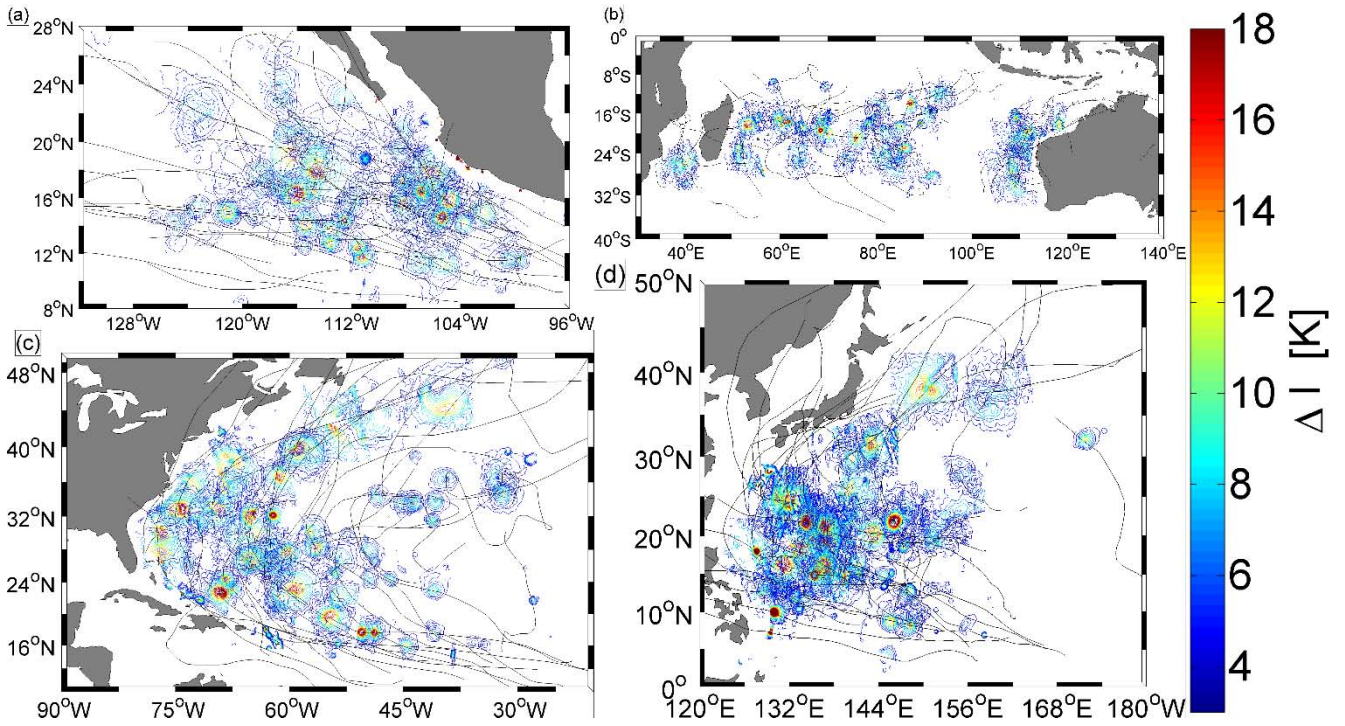
391 the CMORPH data using a 2D Gaussian window of 43 km width. The two closest CMORPH fields in
392 time (before and after a SMOS overpass of a given storm) are linearly interpolated to the SMOS
393 acquisition time.

394 **3 SMOS STORM Database**

395 **3.1 General Characteristics of the SMOS Storm database and analysis subset**

396 A database of SMOS interceptions with Tropical Cyclones has been generated for the satellite data
397 archive period from January 2010 to April 2015 called the "SMOS-STORM database". SMOS intercepts
398 for all TCs within the database were determined by selecting SMOS swaths that intercepted the storm
399 tracks. For each swath, the SMOS L1B data were processed to estimate the residual half-power first
400 Stokes radio-brightness contrasts, ΔI [K], (Eq. 5) at surface level on a 15 km grid. The SMOS retrieved
401 2D wind speed modulus fields based on the first GMF (Reul et al., 2012), hereafter referred to as GMF1,
402 were first computed and co-located with a suite of auxiliary geophysical information (ECMWF, NCEP
403 wind and SST, SSS, etc.). The intercept swaths were then classified by year, basin and storm name. A
404 sub-ensemble of about 300 SMOS swath intercepts with Tropical storms and cyclones was then selected
405 based on how well the swaths intercepted each storms centre (the storm centre and its spatial domain
406 within a radius of ~ 100 -200 km had to be well observed by SMOS). The selection was also based on the
407 quality of SMOS data within each swath (minimum RFI contaminations and undetectable residual
408 uncorrected solar effects...). Only the data of the highest quality possible were selected to physically
409 interpret the L-band contrasts in storms and then invert the data into geophysical parameters (wind, wave,
410 rain, etc.).

411 The distribution of ΔI [K] associated with that sub ensemble of intercepts is shown in Fig. 1. As shown,
412 we selected storms in almost all the active basins of the world oceans showing the variability of brightness
413 temperature contrast distribution in each basin.



414
415

Fig. 1. Contours of storm-surface induced brightness temperature contrasts ΔI [K] estimated from SMOS L-band data for an ensemble of storms in the Eastern Tropical Pacific (a), Southern Indian Ocean (b), North Atlantic (c), and Western Pacific ocean (d) during 2010-2015. The black thin curves indicate the storm tracks. The coloured contours indicate the amplitude of the storm-induced radio-brightness temperature contrasts [K].

421
422

Individual examples of SMOS ΔI for different intensity storms ranging from tropical storms to

423

category 4 on the Saffir-Simpson Wind Scale (SSWS) are shown in Fig. 2. As shown, the shape,

424

magnitude and spatial extent of the storm-induced L-band brightness temperature contrasts demonstrate

425

significant variability around the storm centers. Large asymmetries in the distribution of ΔI around the

426

storm centers are particularly evident for the tropical storms and category 1-2 TCs. The magnitude of the

427

maximum ΔI varies from <12 K for Tropical storms to well above 18 K for Category 4 cyclones on

428

different sides of the storm tracks. Significant drops of ΔI in the storm center region, known to be

429

associated with light winds and low rain, are sometimes visible but are not systematically observed,

430

particularly for those storms showing radii of significant ΔI contrasts that are similar or less than the

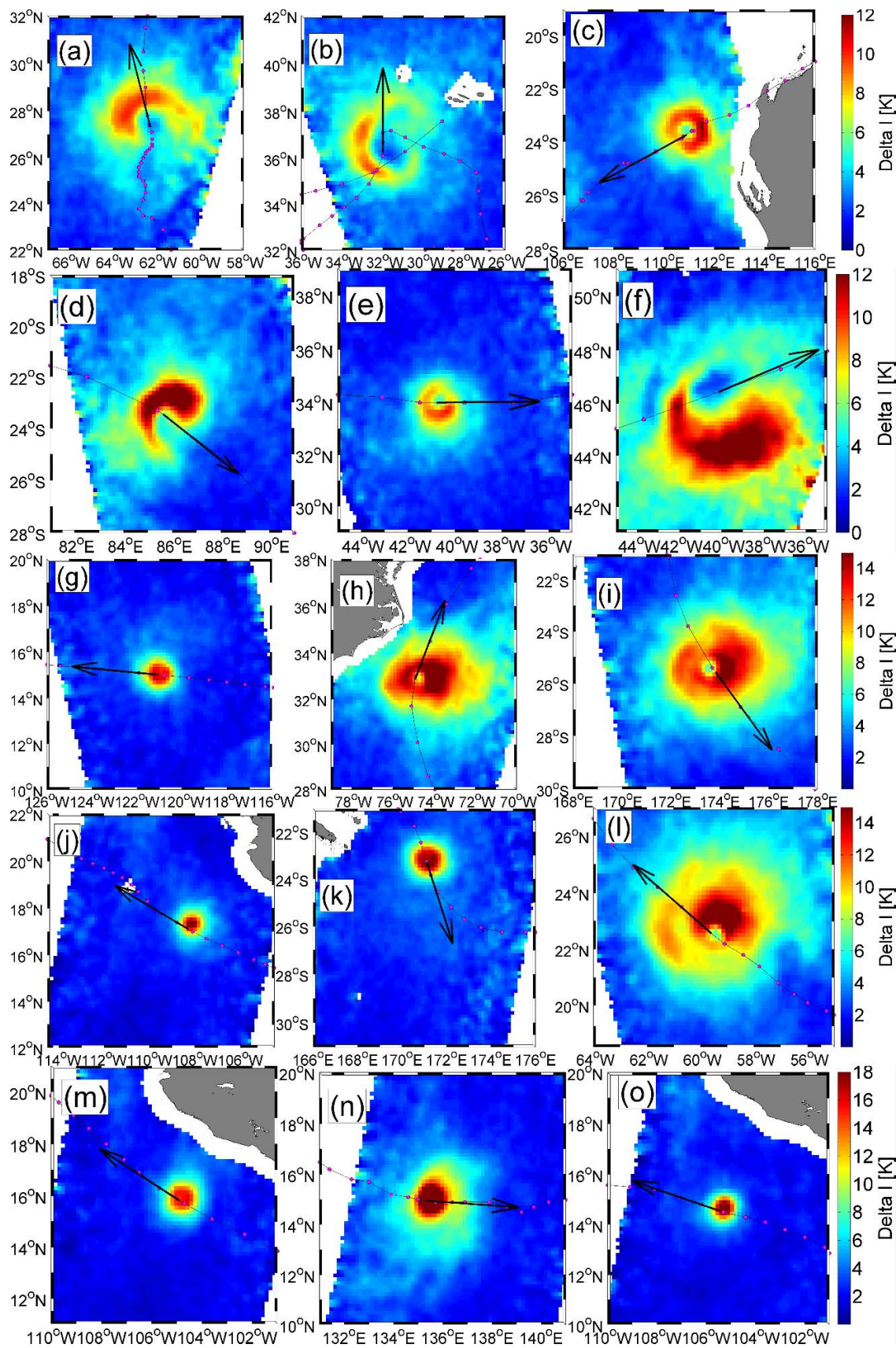
431

SMOS average spatial resolution (~ 43 km). Further classification of SMOS storm intercepts in which

432

the best track one-minute maximum sustained wind speed at the time of SMOS acquisitions was matched

433 to SMOS data resulted in 124 tropical storms, 74 category 1, 41 category 2, 36 category 3, 22 category
 434 4 and 3 category 5 events.



435
 436 **Figure 2:** Examples of SMOS L-band radio-brightness temperature contrasts ΔI [K] measured for tropical Storms
 437 (a,b,c: $35 \leq U_{10} \leq 63$ kts), category 1 TC (d,e,f: $64 \leq U_{10} \leq 82$ kts), category 2 TCs (g,h,i: $83 \leq U_{10} \leq 95$ kts), category 3

438 TCs (j,k,l; $96 \leq U_{10} \leq 113$ kts) and category 4 TCs (m,n,o; $114 \leq U_{10} \leq 135$ kts) on the SSWS. Note that the color-scale
439 range is 0-12 K for TS and category 1, 0-15 K for category 2 to 3 and 0-18 K for category 4 on the SSWS. Each
440 panel represent a domain of about 1000 km width centred on the TC eye. The pink dotted curves show the storm
441 6-hourly best track and the black arrow indicate the storm main propagation direction but not its motion speed.
442

443 **3.2 Statistical characteristics of the L-band brightness contrasts as function of storm intensity** 444 **and sectors**

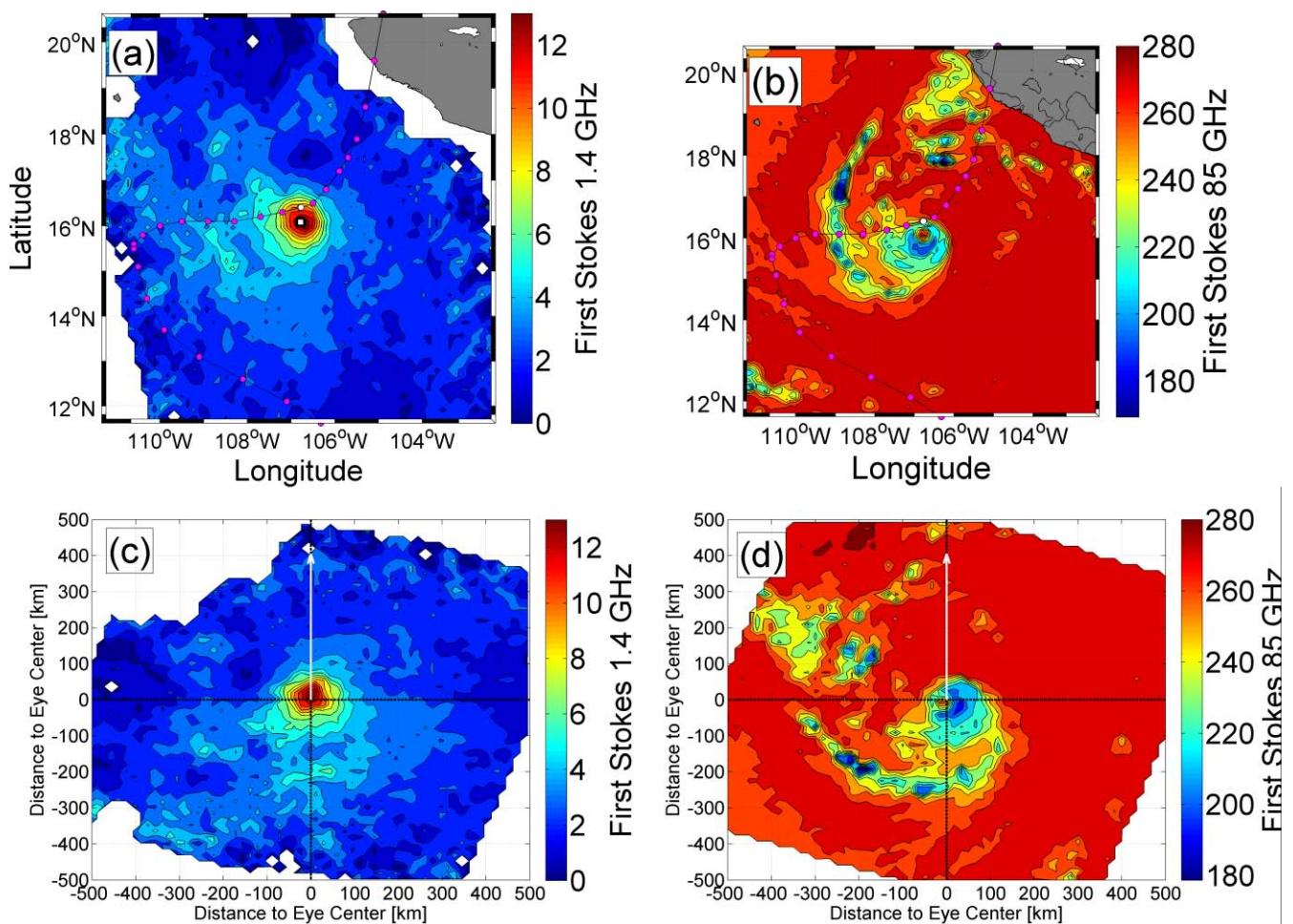
445 **3.2.1 Transformation of ΔI into Storm-centric and common propagation direction frame**

446 To estimate the ‘average’ statistical properties of ΔI and its relationship to storm intensity and storm
447 sector, each SMOS intercept with a storm was processed as follows:
448

- 449 1) The storm center was determined at the time of SMOS acquisition by interpolating linearly in
450 space and time the storm track 6-hourly IBTracks data to the SMOS acquisition time,
451 Microwave 85 GHz data from SSMI15-16-17-18, TMI or AMSRE that were acquired within less
452 than ± 1 hour from SMOS intercepts were then used to check the determination of the storm center
453 locations estimated from the best-track data. If 85 GHz images were available within less than
454 \pm half an hour from SMOS, the location of the storm centre was determined using these data.
455 Otherwise, the storm centre location was bi-linearly interpolated in space and time from the two
456 closest 85 GHz observations acquired just before and after SMOS acquisition. A visual check
457 was further performed to check consistency between SMOS-derived storm centre location, best-
458 track location, and 85 GHz interpolated locations. In case of a significant mismatch, the centre
459 determined from the 85 GHz data was used by default. Fig. 3 shows an example for a SMOS
460 intercept with hurricane Jova on 10 October 2011 as it developed in the eastern Pacific into a
461 Category 3 storm before it landed in western Mexican coasts. SMOS intercepted the storm at
462 12:32 Z. The best-track linearly-interpolated storm centre location at that hour (Fig. 3, top left) is
463 found at $\sim [16.35^\circ\text{N}, 106.8^\circ\text{W}]$ which is $\sim 0.3^\circ$ north of the observed maximum in SMOS
464 brightness temperature contrast $[16.05^\circ\text{N}, 106.78^\circ\text{W}]$. If the best-track determined centre location
465 is assumed to be the actual storm centre, then the SMOS ΔI distribution, as observed, would be

466 strongly asymmetric with a significant right-hand displacement of the maximum ΔI with respect
 467 the storm track. An 85 GHz image from SSMIS-17, acquired within 28 minutes of the SMOS
 468 data reveals that the storm eye was actually centred at [16.08°N, 106.78°N], consistent with the
 469 centroid of SMOS ΔI observations. This example illustrates the challenge to accurately and
 470 consistently determine storm eye centres – a necessary requirement if the statistical properties of
 471 the ΔI in a storm-centric frame are to be used to determine potential asymmetries around the
 472 different storm sectors.

473
 474



475 **Figure 3:** (a): SMOS ΔI estimated over Category 3 TC Jova at 12:32 Z on 10 October 2011. The pink dotted
 476 curve shows the Best Track of Jova; the white filled dot and square indicate the eye location estimated by linear
 477 interpolation of the Best Track data at SMOS acquisition time and from the closest 85 GHz acquisition. In this
 478 case, the latter is obtained from SSMIS/17 imagery at 12:59 Z (b). (c) and (d): same fields as top panels but
 479 provided in a storm-centric frame of 1000 km² and rotated with respect the storm heading “North Up” that is shown
 480 as a white arrow.
 481
 482

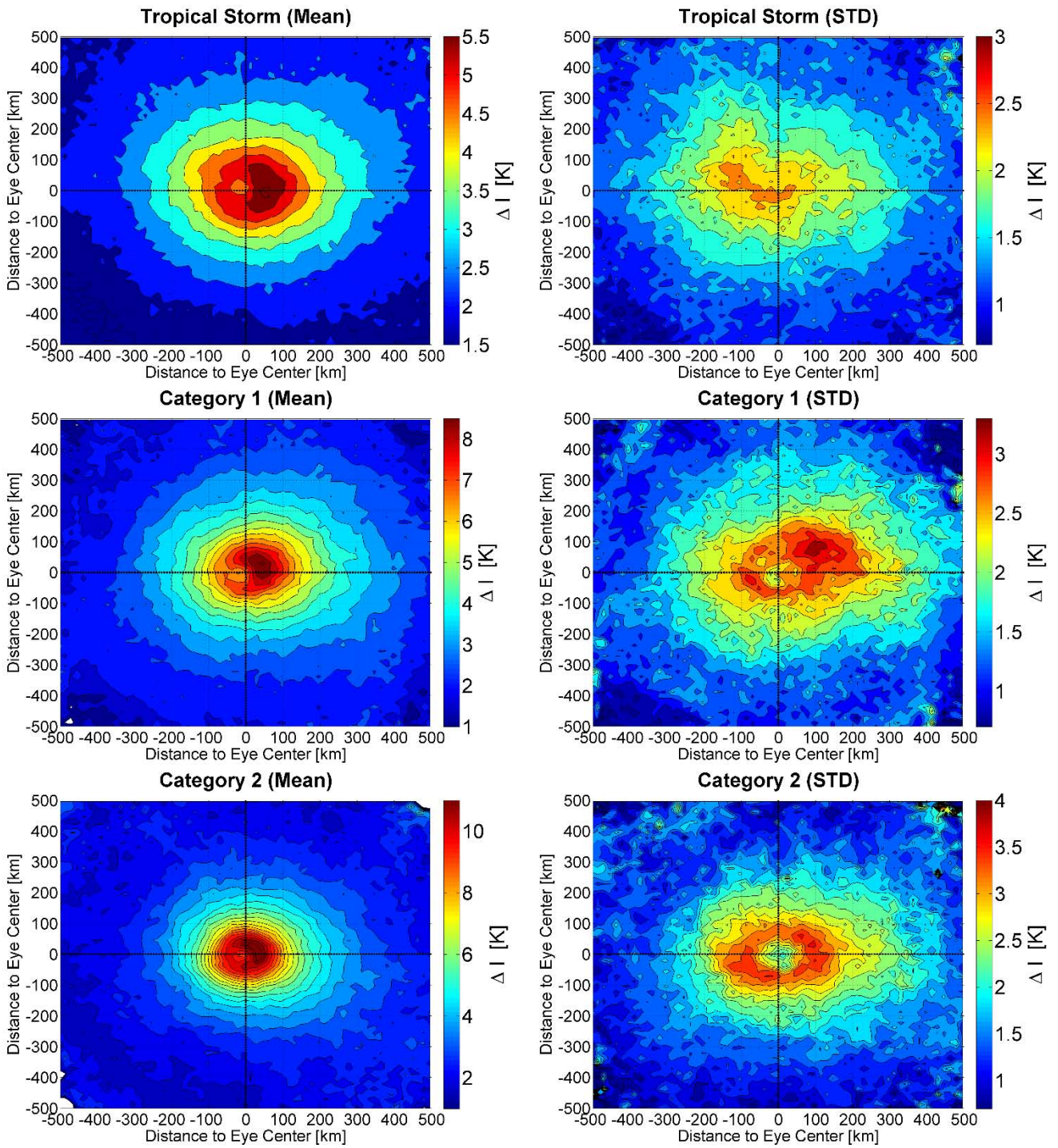
483 For convenience, we arbitrarily choose to rotate all ΔI distributions to a “northern-hemisphere” common
484 coordinate system display geometry (see example for Jova in Fig. 3, which was actually heading towards
485 the northeast at the SMOS acquisition time). Using the storm centre locations estimated at the SMOS
486 acquisition times all ΔI data were further re-gridded at 15 km spatial resolution on a storm-centric
487 coordinate system with west-east and north-south axes spanning a spatial domain of 500 km on each side
488 of the storm centre. The heading of the storm translation motion was then estimated from the best-track
489 interpolated data at the SMOS acquisition time and the ΔI fields were rotated to align all storm translation
490 directions to a common axis. Note that the fields were reflected around that axis (i.e. to flip the wind
491 fields in left/right direction) for the southern-hemisphere storms to account for the different veering wind
492 directions in both hemispheres. SMOS winds were not adjusted to account for the storm translation speed
493 but only rotated based on the motion direction.

494 **3.2.2 Statistical distributions of ΔI as function of storm intensity and sectors**

495

496 We compute the 2D distributions of the mean and standard deviation of L-band ΔI as function of the
497 different Saffir-Simpson TC categories for all storms in our database and plot the result in Fig. 4 using
498 storm-centric coordinates (ie. all storms have been consistently rotated to point “North Up”). The mean
499 distributions of ΔI coherently increase with the increasing TC intensity. The radii within which the
500 brightest ΔI values are found for each category reduces as the storm intensity increases, consistent with
501 the reported evolution of the highest surface wind distribution in TCs (Holland, 1980, Chavas et al.,
502 2015). A remarkable feature of the mean ΔI fields is that the maxima are systematically found on the
503 right-hand side quadrant of the storms. This is also consistent with the reported asymmetric structure of
504 the wind and wave fields in TC where the maximum in wind speed and sea surface heights occur in the
505 right-hand quadrant of the storm (in the northern-hemisphere) because of the relative wind created by a
506 translating storm (Uhlhorn et al. 2014; Rogers and Uhlhorn, 2008; Molinari and Skubis, 1985). Except
507 for the lower intensity tropical storm case, the standard deviation (STD) of ΔI fields also reflect similar
508 characteristics to the mean field. For TC categories 1-5, the STD shows a quasi-annular distribution

509 around the storm centre, local minima at the storm centre - a signature of the relatively calm eye of a TC,
510 and local maxima in the right-hand quadrant of the storms.

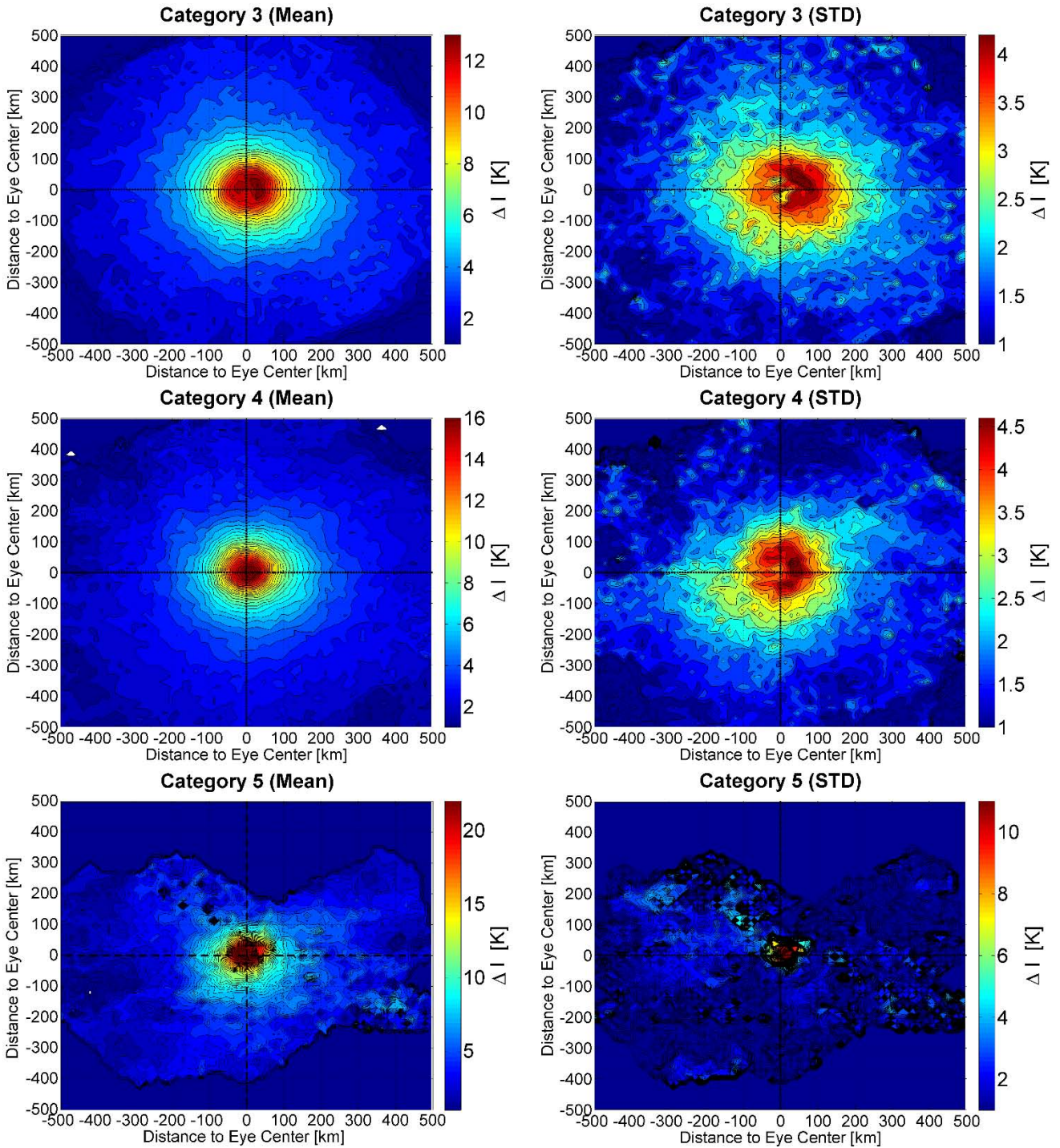


511

512 (see legend and rest of the figure next page)

513

514



515
516
517
518
519
520
521
522
523
524
525
526

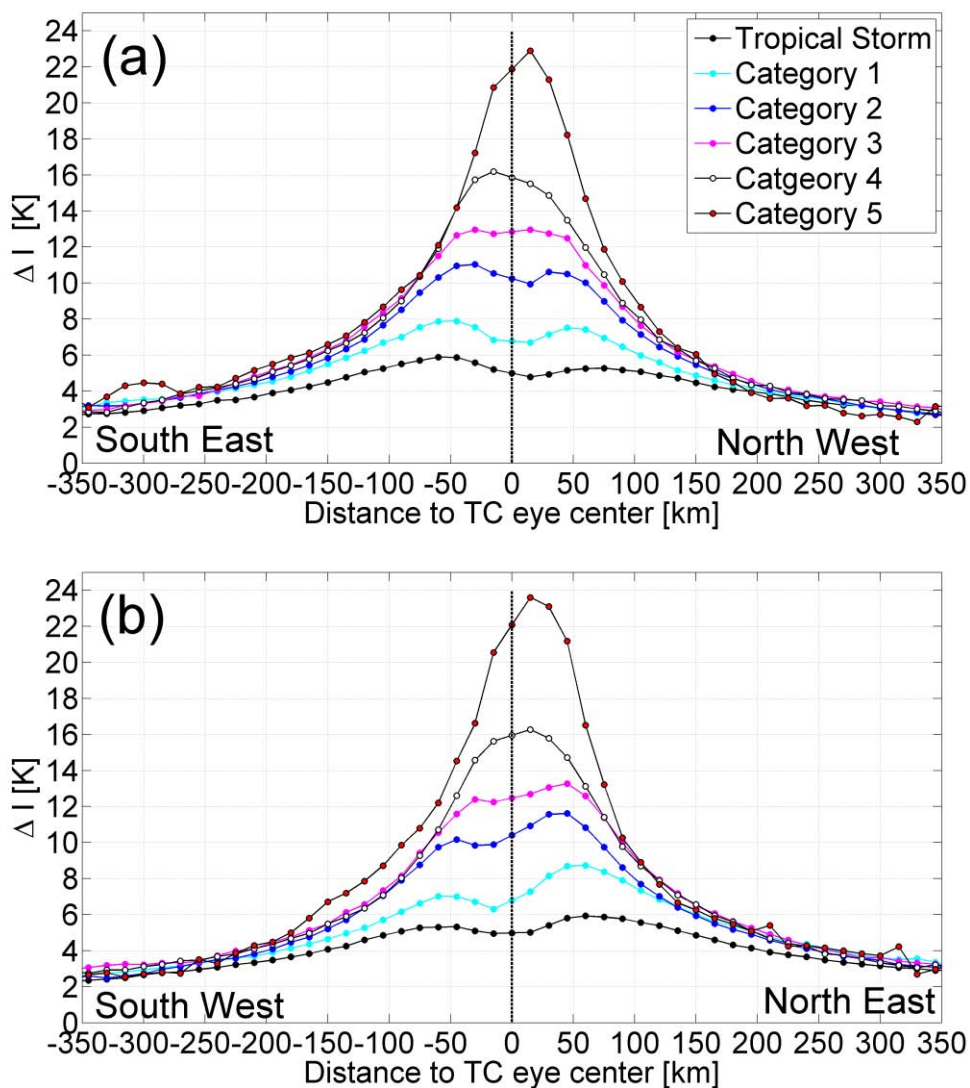
Fig. 4. Storm centric contours of the mean (left panels) and standard deviation (right panels) of the L-band radio brightness half power contrast (ΔI [K]) as function of storm sector and intensity. The wind intensity is ranging from tropical storms (top panels, $35 \leq U_{10} \leq 63$ kts), Category 1 TCs (second panels from top, $64 \leq U_{10} \leq 82$ kts), Category 2 TCs (3rd panels from top, $83 \leq U_{10} \leq 95$ kts), Category 3 TCs (4th panels from top, $96 \leq U_{10} \leq 113$ kts), Category 4 TCs (5th panels from top, $114 \leq U_{10} \leq 135$ kts) and Category 5 (bottom panels, $U_{10} > 135$ kts). Contours range from 1 to 28 K in steps of 0.5 K for the mean and from 0 to 10 K in steps of 0.2 K for the standard deviation. Note that the colour scale range is changing from top to bottom panels.

527

Fig. 5 highlights the storm quadrant and intensity dependencies of SMOS ΔI for all tropical cyclones in our database. The mean brightness contrast is clearly seen to monotonically increase with

528 storm intensity within a ~ 200 km radius from the storm centre. The mean ΔI amplitude ranges from about
 529 5 K for tropical storms up to ~ 24 K for the most intense category 5 cyclones. There is no evidence of ΔI
 530 saturation and the brightness increases between TC categories by ~ 3 -4 K. The step change from Category
 531 4 to Category 5 is more significant (~ 8 K) but this result is not robust given that only 3 Category 5 events
 532 were intercepted by SMOS. There is evidence of a right-hand-side asymmetry and the maxima of ΔI is
 533 always found in the north-east and south-east quadrants. The typically calm inner-core wind structure is
 534 difficult for SMOS to resolve when the radii of maximum wind is less than ~ 43 km (the mean spatial
 535 resolution of the SMOS data) and is most noticeable for the intense wind conditions (category 4 and
 536 above) where the radial structure of the TC is typically compressed.

537



538 **Fig. 5.** Mean radial distribution of the storm-induced L-band half-power radio-brightness contrasts (ΔI [K]) as
 539 function of storm intensities (colors) given by the Saffir Simpson wind Scale (a) from the South East to the North
 540 West storm quadrants and (b) from the South West to the North East storm quadrants.

542

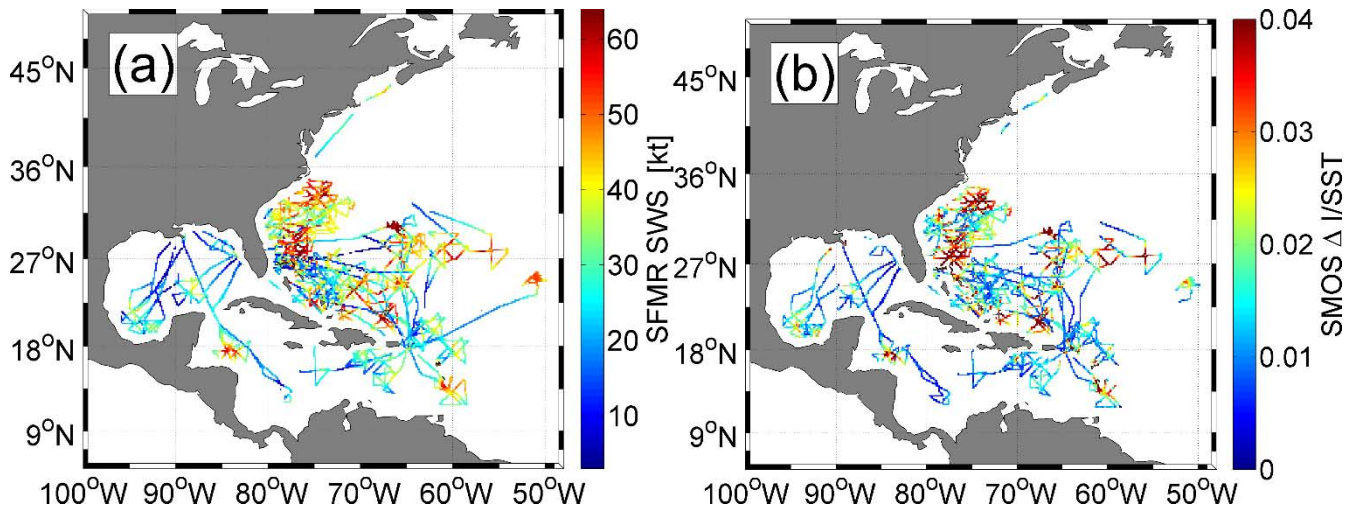
543 **4 A revised L-band Geophysical Model Function**

544

545 The bi-linear GMF relationship ‘GMF1’ between ΔI and the 10 m height surface wind speed
546 U_{10} proposed in Reul et al. (2012) has been inferred solely from observations acquired over a single
547 north-Atlantic hurricane event (Category 4 hurricane Igor in 2010). Using the co-located SMOS, SMFR
548 flight track data and analysed 2D H*Wind fields within our SMOS-STORM database, we have revised
549 the original GMF, hereafter referred to as ‘GMF2’, as discussed in the following sections.

550 **4.1 Systematic comparisons between SMOS and SFMR**

551 Considering the SMOS-STORM database, we found 64 co-locations between SMOS and SFMR flight
552 tracks in ~ 30 TCs over the period 2010-2014. A first SMOS-SFMR paired database was constructed by
553 selecting co-located data with time differences (Δt) between both acquisitions of less than ± 12 hours to
554 provide a large number of pairs. A subset only including pairs with $|\Delta t| < 6$ hours was further used to
555 establish statistical relationships between SMOS ΔI and SFMR wind speed. If the central time lag, Δt ,
556 between SMOS and SFMR data as the aircraft flew over the eye region exceeded ± 0.5 h, the storm center
557 displacement between the aircraft and satellite acquisitions could have been significant. To adjust for
558 storm motion when $|\Delta t| > 0.5$ h, SFMR tracks were spatially translated (without rotation) from the original
559 storm centre location detected in SFMR data to the storm centre location evaluated at the SMOS time.
560 The SMOS ΔI were then further bi-linearly interpolated in space to match the SMFR data at ~ 3 km
561 intervals along each SMFR flight track. The geographic distribution of the ensemble of co-located SMOS
562 and SFMR flight tracks is shown in Fig. 6. Only intercepts with storms that developed in the North-
563 Atlantic and Gulf of Mexico have been processed.



564

565 **Fig. 6.** (a) Ensemble of SFMR tracks and associated Wind Speed [knots] used for SMOS-SFMR
 566 comparisons, and (b) SMOS L-band excess emissivity (Δe) contrasts co-located with SFMR flights.

567

568 Given the varying SST conditions encountered for all the storms, in what follows, the SMOS ΔI will be

569 now expressed in terms of the storm wind-excess emissivity:

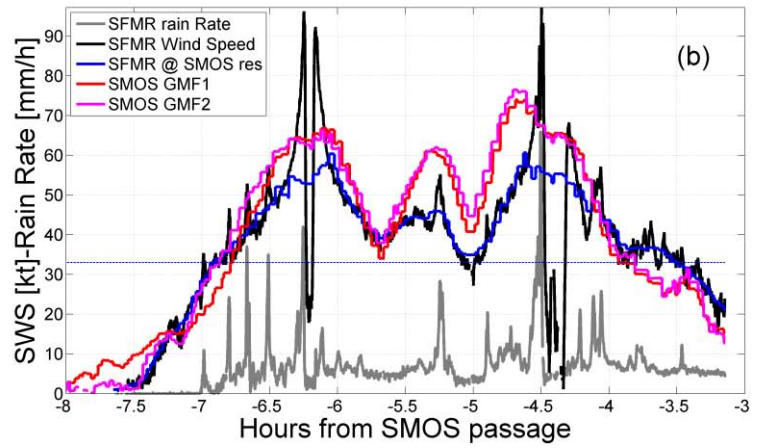
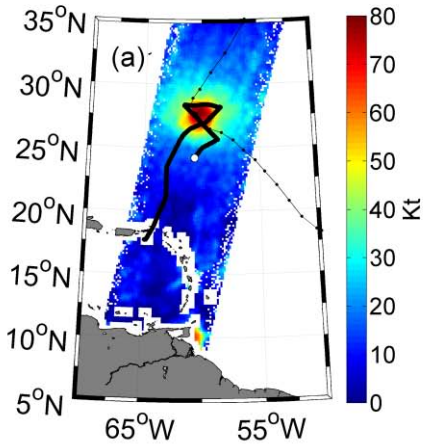
570
$$\Delta e = \Delta I / sst \quad (6)$$

571 Fig. 6 shows that the relative distribution of wind speed measured by SFMR closely match co-located
 572 SMOS Δe , with brightest spots in SMOS Δe data almost always spatially coincident with the highest
 573 wind regions retrieved along SMFR flights.

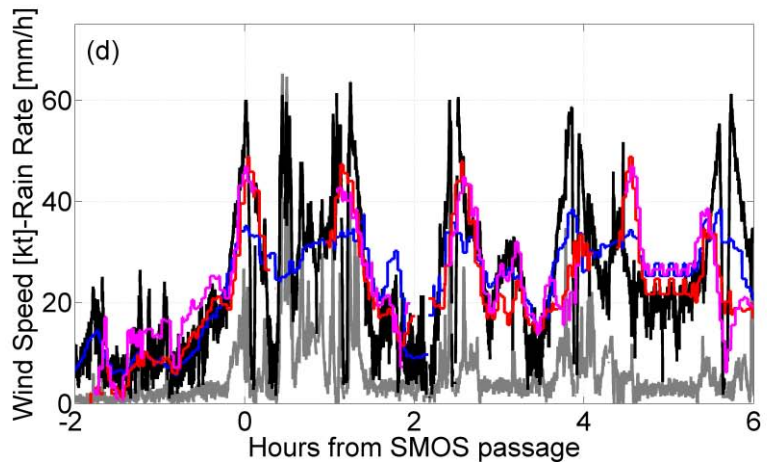
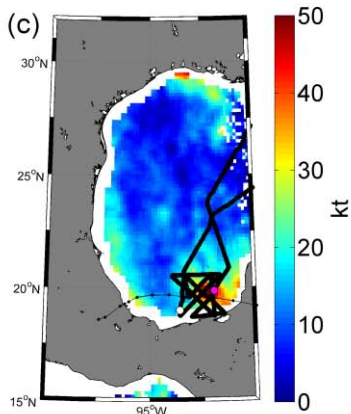
574 As a baseline to compare our GMFs, Fig. 7 show representative examples of the co-located surface wind
 575 speed retrieved from SMOS using the first GMF (Reul et al., 2012) and second GMF (see below Eq. 7,
 576 section 4.2) compared to SFMR estimates. For this comparison SFMR surface wind speed data were
 577 spatially averaged along their track using a Gaussian running window of ~ 43 km width (blue curves) to
 578 better match spatial resolution of SMOS multi-angular data. Both spatially filtered and nominal
 579 resolution data are shown for comparisons. The SMOS wind estimates provide a good match to the
 580 smoothed SFMR surface wind speed measurements. For the intermediate wind speed range of $\sim 30 - 60$
 581 kt mismatches and biases are evident that are independent of the time lags between SMOS and SFMR
 582 measurements. In high wind gradient regions and zones of high spatial-resolution variability (eg. around
 583 the TC eye) detailed structure is not evident in the SMOS data due to the low spatial resolution of the

584 SMOS instrument. Nevertheless, the match is particularly good in the highest wind speed range in general
585 (e.g., see Fig7.f and h).

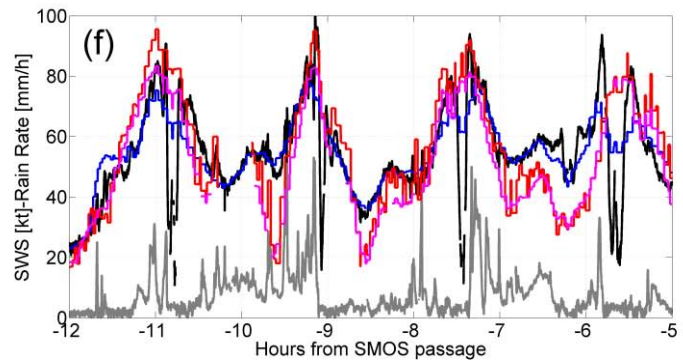
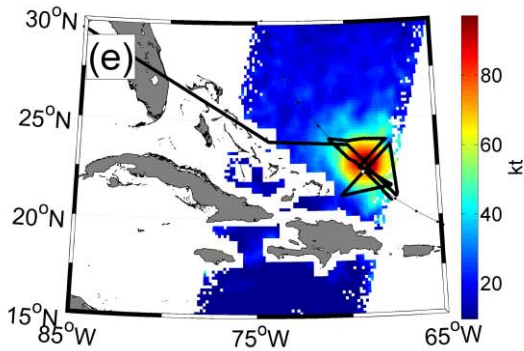
586



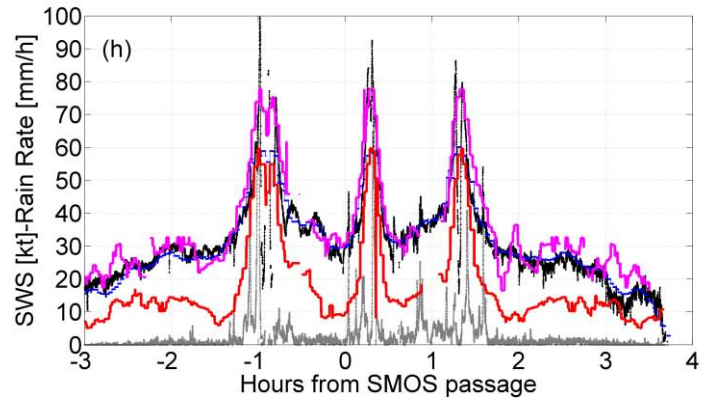
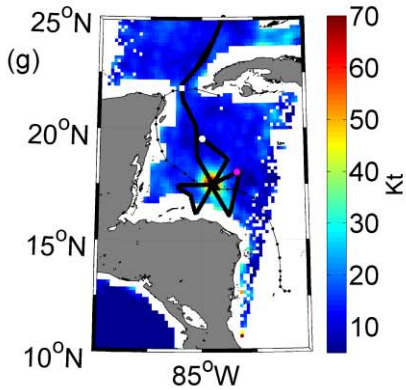
587



588

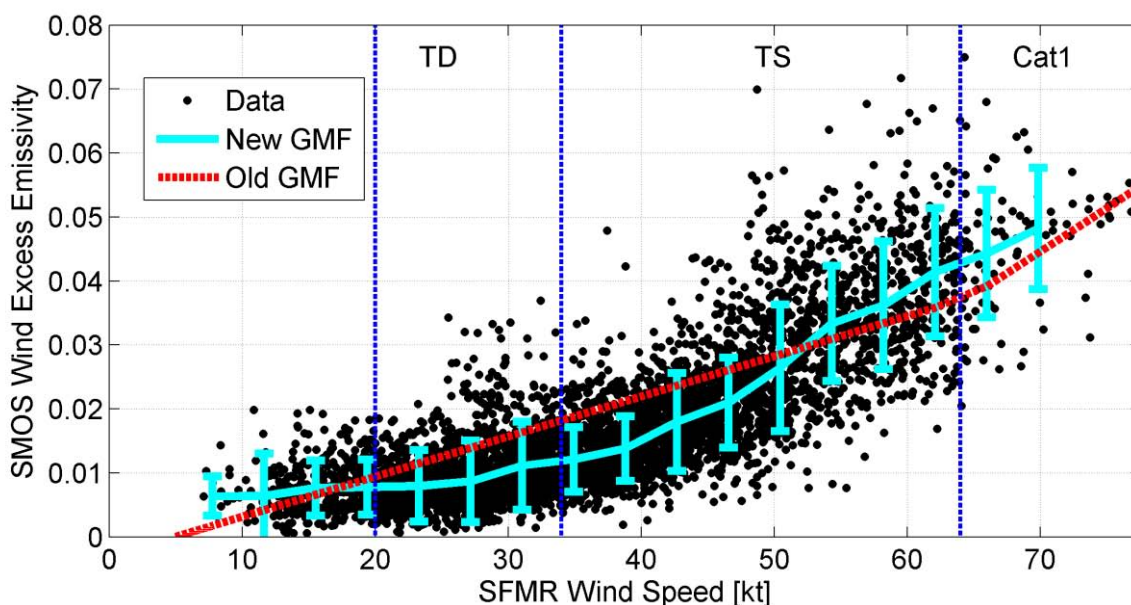


589



590 **Fig. 7.** (a,c,e,g) superimposed SMOS retrieved wind speed using the GMF of Reul et al (2012, color in
 591 knots) and SFMR track (black thick curves) for hurricane Daniele the 28 August 2010 (a), hurricane Karl
 592 on 16 September 2010 (c); hurricane Earl on 31 August 2010 (e) and hurricane Rina on 25 Oct 2011.
 593 The thin dotted curves indicate the storm tracks. b,d,f,h: corresponding time series of the SFMR retrieved
 594 wind speed in m/s (black curve) and rain rate in mm/h (grey curve) at nominal resolution along aircraft
 595 track (~3 km). The SFMR retrieved wind speed has been spatially averaged with a running window of
 596 43 km width along track (corresponding to the mean resolution of SMOS interferometer pixels) is shown
 597 in blue. The retrieved wind speed from SMOS is shown in red using GMF1 and in magenta using GMF2.
 598 The x-axis shows the time lag between SFMR acquisitions and SMOS ones.
 599

600 To minimize the potential impact of structural evolution of the storm between SMOS and SFMR
 601 acquisition times, we further selected only those data pairs with $|\Delta t| < 6$ h to derive a new GMF. Biases
 602 in SFMR wind data induced by high rain-rates were also corrected according to Klotz and Uhlhorn
 603 (2014). Fig. 8 shows the storm-induced Δe as function of the co-located SFMR wind speed (spatially
 604 smoothed at SMOS resolution and obeying the previous time lag constraint). The median and standard
 605 deviation of the ΔI values per 10 kt-width bins of SFMR wind speed are also provided. For comparison,
 606 we show the bi-linear GMF1 from Reul et al., 2012.



607 **Figure 8:** SMOS storm-induced excess L-band emissivity, Δe , as function of co-located SFMR wind
 608 speed for an ensemble of 64 SMFR flights in the Gulf of Mexico and western Atlantic ocean. The time
 609 lags between both observations never exceed 6 h. The red line indicate the first bi-linear GMF proposed
 610 in Reul et al. (2012). The cyan curve indicates the mean wind-excess emissivity per 10 kt-width bins and
 611 the vertical bars indicate ± 1 standard deviation of the emissivity within each bin.
 612

613
 614
 615 As can be seen, while rather close to the first bi-linear GMF estimate, the new fit based on SMOS and
 616 SFMR wind speed co-located pairs is a nonlinear function of the wind speed. In particular, the new GMF

617 shows that the storm-induced excess emissivity is almost wind-speed independent for winds below ~20
618 kt. In the intermediate wind speeds ranging from 20 to 50 kt, the new GMF lies below the old linear
619 relationship indicating an underestimation of the retrieved wind speed from SMOS data using the linear
620 empirical law or Reul et al (2012). This is particularly evidenced in Fig 7h, which shows an
621 underestimated SMOS retrieved wind in that range using GMF1, further corrected using GMF2. Note
622 for this particular case that most of the differences between GMF1 and GMF2 is related to the use of
623 climatological SSS for GMF1 and SMOS SSS for GMF2. In the highest wind speed regime (>50 kt), the
624 new GMF function shows a systematically higher value than the linear approach. It is interesting to note
625 that the new GMF exhibits similar dependencies with wind speed when compared to the excess
626 emissivity vs. wind speed law deduced for the C-band SFMR data (Uhlhorn et al. 2007; Klotz and
627 Uhlhorn, 2014).

628 **4.2 Systematic comparisons between SMOS and H*WIND**

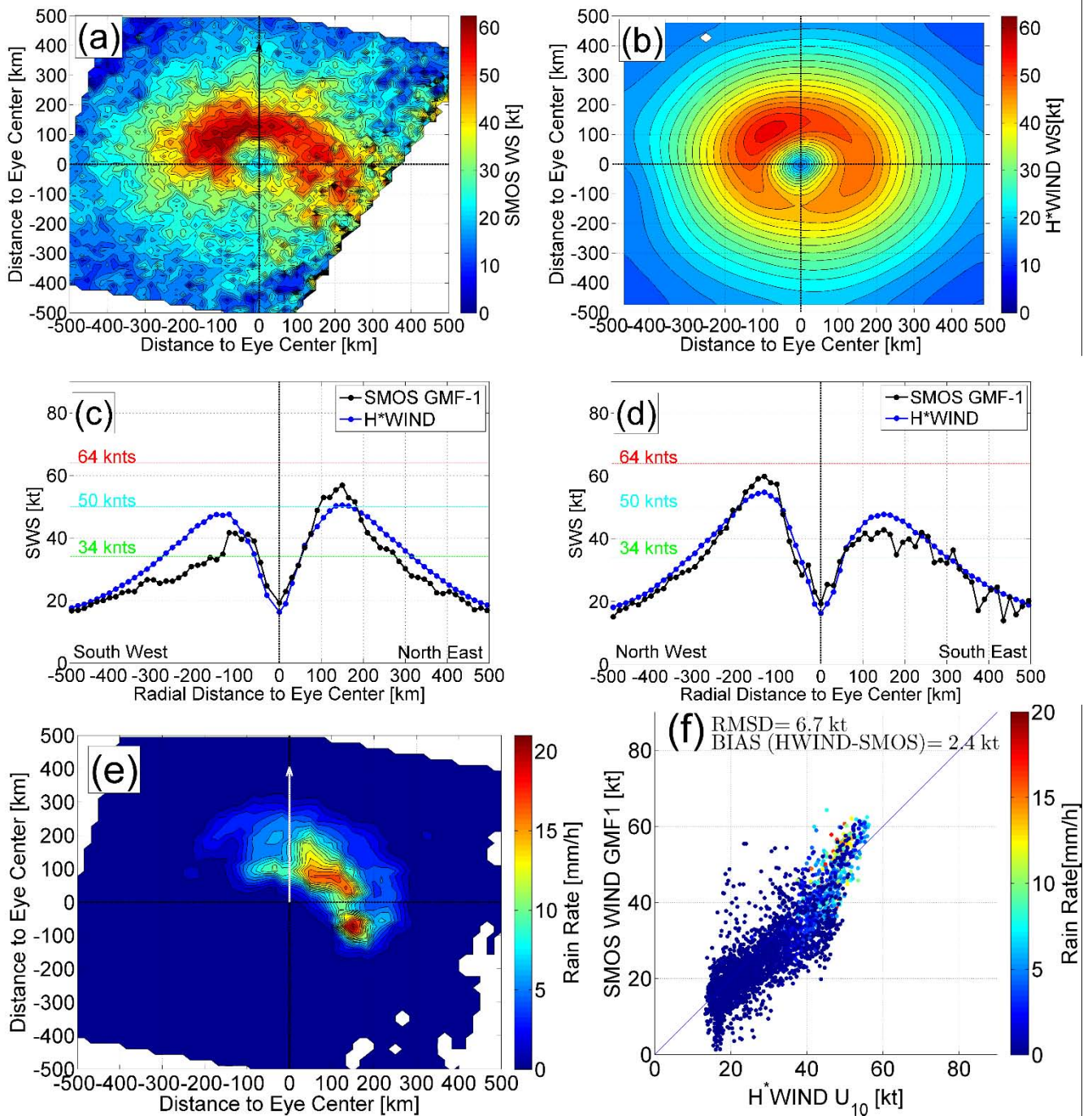
629 The SMOS-SFMR co-located dataset (Fig. 7) shows that the Reul et al (2012) linear GMF1 retrieves
630 relatively accurate surface wind speed values from SMOS observations in TCs. However, Fig. 8 also
631 highlights a slightly more non-linear behaviour of the Δe as function of surface wind speed than Reul et
632 al. (2012) which was based on a single TC, particularly in the intermediate (20 to 40 kt) and high (>50
633 kt) wind speed ranges that would result in under and over estimation of the surface wind speed,
634 respectively.

635 Given the time-lag constraints in the SMOS-SFMR data co-location and data selection used when
636 building the GMF, inevitably only a small number of match-ups were available in the highest wind speed
637 regime with very little data above hurricane force (>64 kt). To increase our confidence in the statistical
638 reliability of the GMF and to increase the quantity of co-located pairs at the highest winds, we constructed
639 an extended database of SMOS Δe , retrieved SMOS surface wind speed (using Reul et al (2012) GMF
640 as a first guess) and H*WIND 2D surface wind speed fields. 30 cases were found for which either SMOS
641 data were available within $< \pm 0.5$ h from an H*WIND or when the two closest H*WIND wind fields in

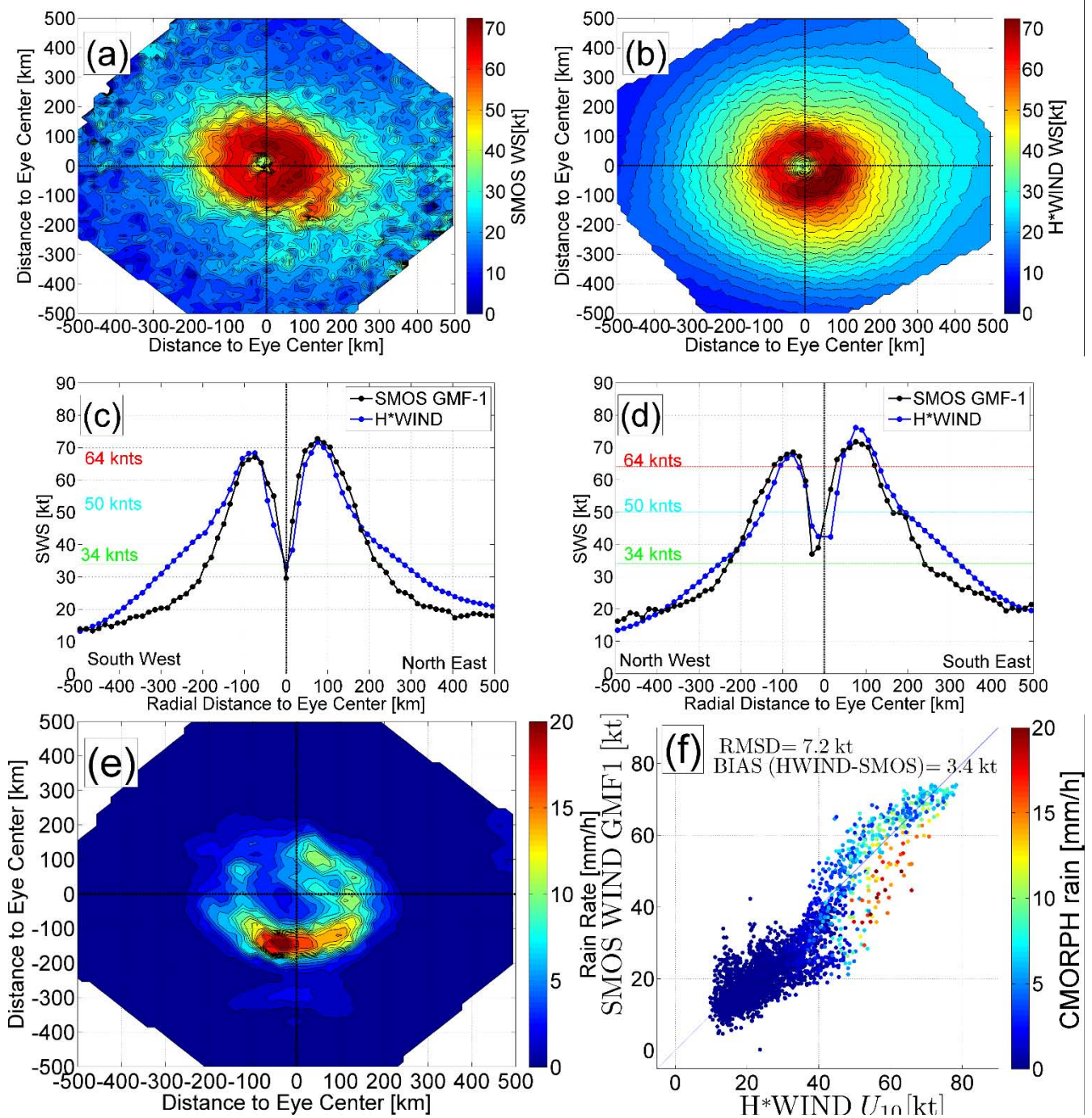
642 time (before and after a SMOS overpass of a storm) was available within 6 h. In the latter case, an
643 interpolation in time of the two closest storm-centric H*WIND SWS fields was performed at the SMOS
644 time.

645 For illustration, Fig. 9 and 10 show two examples of SMOS/H*WIND comparisons. Fig. 9 shows the
646 results for Hurricane Leslie as it developed to a TC on 7 September 2012 at 22:19 Z. The RMS difference
647 between SMOS and H*WIND SWS fields is ~7 kt. As shown, the structure of both wind fields are very
648 consistent, with maximum winds found in the north-west quadrant at a radial distance of about 150 km
649 with the maximum wind radii at 34 and 50 kt matching closely between both products in the NW and SE
650 quadrants. Nevertheless, small residual biases are seen in the two other quadrants, with SMOS winds
651 lower than H*WIND and a smaller 34kt radius in the SW quadrant

652
653



654
 655 **Fig. 9.** (a) Surface wind speed retrieved from SMOS (GMF of Reul et al (2012)) in a storm centric coordinate
 656 system for hurricane Leslie on 7th September 2012 at 22:19. (b) H*WIND fields interpolated at SMOS acquisition
 657 time and spatially averaged at 43 km resolution. (c) Mean radial distribution of the SMOS (black) and H*WIND
 658 (blue) surface wind speed from the SW to the NE storm quadrants, and (d) from the NW to the SE storm quadrants.
 659 (e) CMORPH rain rate at SMOS acquisition time. (f) SMOS retrieved wind speed as function of H*WIND with
 660 color indicating the rain rate from CMORPH.
 661
 662
 663
 664
 665
 666



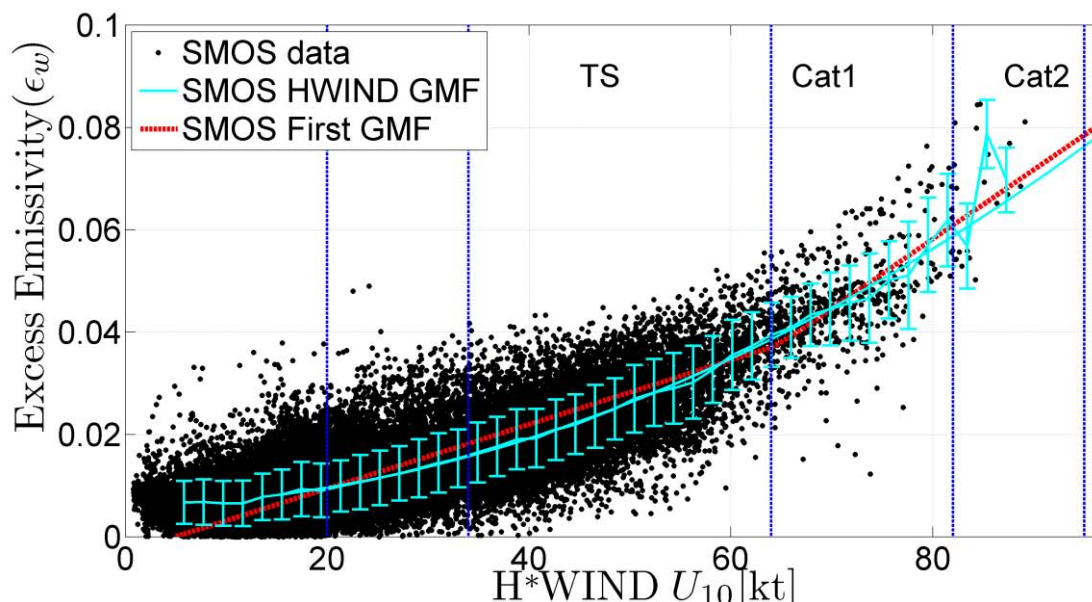
667
 668
 669
 670
 671
 672
 673
 674
 675

Fig. 10. Same caption as Fig.9 except for the case of hurricane Katia on the 6th September 2011 at 09:35 Z.

SMOS winds are slightly higher than H*WIND in the NE quadrant at radial distances between 100 and 200 kms (Fig. 9 c,d). Considering the co-located CMORPH data, the rain rate reached more than 20 mm/h at some locations in the highest wind speed band found in this quadrant corresponding to retrieved SMOS winds slightly higher than H*WIND (Fig. 9 e, f).

676 The second example (Fig 10) shows the case of Hurricane Katia as it reached a Category 2 intensity.
 677 Here again, the match between both SMOS and H*WIND wind speed fields is rather good in general
 678 (RMS ~ 7.2 kt), with consistent estimates of the maximum wind radius and value (around 80 kt), and of
 679 the 50 and 64 kt wind radii. However, SMOS retrieved winds at 34 kt exhibit a slightly smaller wind
 680 radii than the H*WIND product. This is consistent with the behaviour expected from the bilinear GMF
 681 according to SMOS/SFMR matchups. Contrary to the case of hurricane Leslie (Fig.9), the intense rain
 682 region (with rain rates >20 mm/h) is now associated with underestimated SMOS winds with respect
 683 H*WIND. As the impact of precipitation is inconsistent it appears that this is not the principal process
 684 responsible for the observed biases in SMOS winds versus H*WIND (see Fig. 9 and Fig. 10 e, f).

685



686

687 **Fig. 11:** Wind Excess emissivity $\Delta\epsilon$ as function of co-located H*WIND wind speed for an ensemble of
 688 storms in between 2010 and 2013. The red curve illustrates the SMOS GMF of Reul et al (2012). The
 689 cyan curve show the new 'average' GMF function derived in this paper based on the SMOS and H*WIND
 690 paired data. $\Delta\epsilon$ data have been averaged into bins of H*WIND winds at 5 knots intervals with the vertical
 691 error bar indicating ± 1 standard deviation of the $\Delta\epsilon$ within each wind speed bin.

692

693

694 We use 30 2D fields of co-located SMOS ΔI and H*WIND (an alternative and spatially complete
 695 'ground-truth' dataset) and re-analysed the SMOS wind GMF. Fig. 11 shows the $\Delta\epsilon$ as function of
 696 H*WIND 1-minute sustained winds that have been spatially averaged to 43 km corresponding to the
 697 mean SMOS spatial resolution. In between 20 kt and ~ 50 kt, the GMF derived based on H*WIND fields

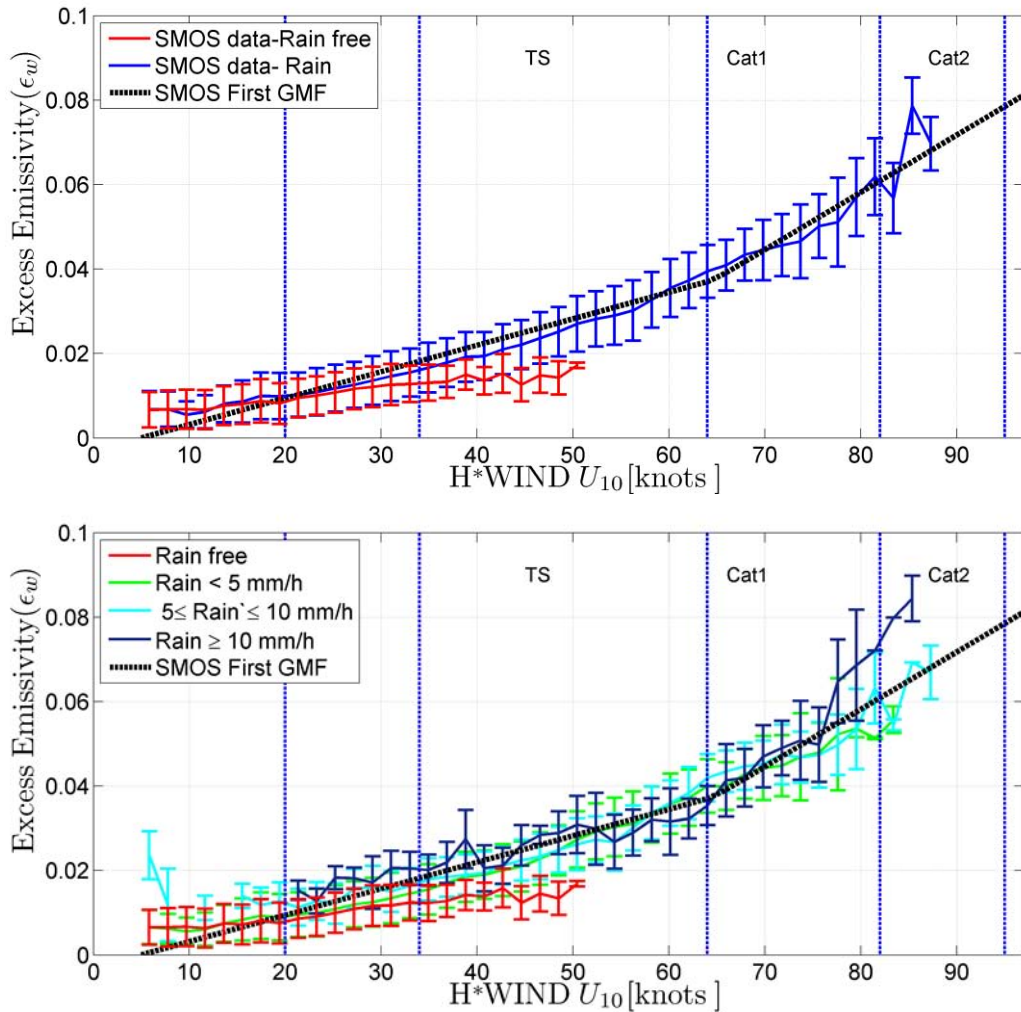
698 shows a very similar structural form to the GMF derived using only SFMR data: it is systematically found
699 lower at a given wind speed than the bi-linear GMF1 of Reul et al (2012). This might be expected as
700 SFMR data are used as key input data to derive the H*WIND analyses. In the wind speed regime over
701 50 kt, the H*WIND derived GMF is very similar to the GMF of Reul et al (2012), which was not the
702 case for the SFMR matchups. At wind speeds $< \sim 10\text{-}15\text{kt}$ the new GMF shows little sensitivity. A
703 quadratic fit through the data give the following GMF function for the half-power L-band storm-induced
704 brightness temperature contrast as function of the H*WIND 1-minute sustained surface wind speed
705 averaged at SMOS spatial resolution:

$$706 \quad \Delta I(U_{10}) = SST \cdot (2.7935 \times 10^{-5} U_{10}^2 + 6.8599 \times 10^{-5} U_{10} + 0.0059) \quad (7)$$

707 As H*WIND and SFMR-based fits are very similar in the low to moderate wind speed range and, given
708 the fact that the H*WIND GMF includes the SFMR data and provides a much larger number of paired
709 data for the high wind regime, we use (Eq. 7) as the new reference GMF for retrieving surface winds
710 from SMOS L-band radio-brightness contrasts data. Hereafter, we referred to this new GMF as GMF2.

711 **4.3 Potential Impact of Rain**

712 The previous GMFs were built assuming that there is no impact of rain and sea state on the L-band
713 contrasts. Using CMORPH co-located 2D observations, all data used to build up the H*WIND derived
714 GMF have been characterized in terms of rain rate. Fig. 12 (top) shows the bin-averaged Δe as function
715 of wind speed for rain free and rainy conditions. Unfortunately, data showing rain-free conditions are
716 only available up to a wind speed of 50 kt. For surface winds of >20 kt, the rain free Δe at a given wind
717 speed is systematically lower than the equivalent Δe measured in rainy-conditions. The differences in Δ
718 e between rainy and non-rainy conditions reach a maximum of ~ 0.01 at 50 kt, which for a typical SST of
719 28°C would translate into a 3 K bias in ΔI due to rain.



720

721
722

723 **Fig. 12:** Potential effects of rain on the excess L-band emissivity Δe in storm conditions. Top: GMF
724 deduced from the SMOS and H*WIND matchups with rain rate provided from CMORPH=0 (red) and
725 rain rate > 0 (blue). Bottom: similar caption than for the top plot except that the data are now classified
726 by ranges of rain rate (RR): RR=0 (red), 0<RR≤5 mm/h (green), 5mm/h<RR≤10 mm/h (cyan) and
727 RR>10 mm/h. (blue).

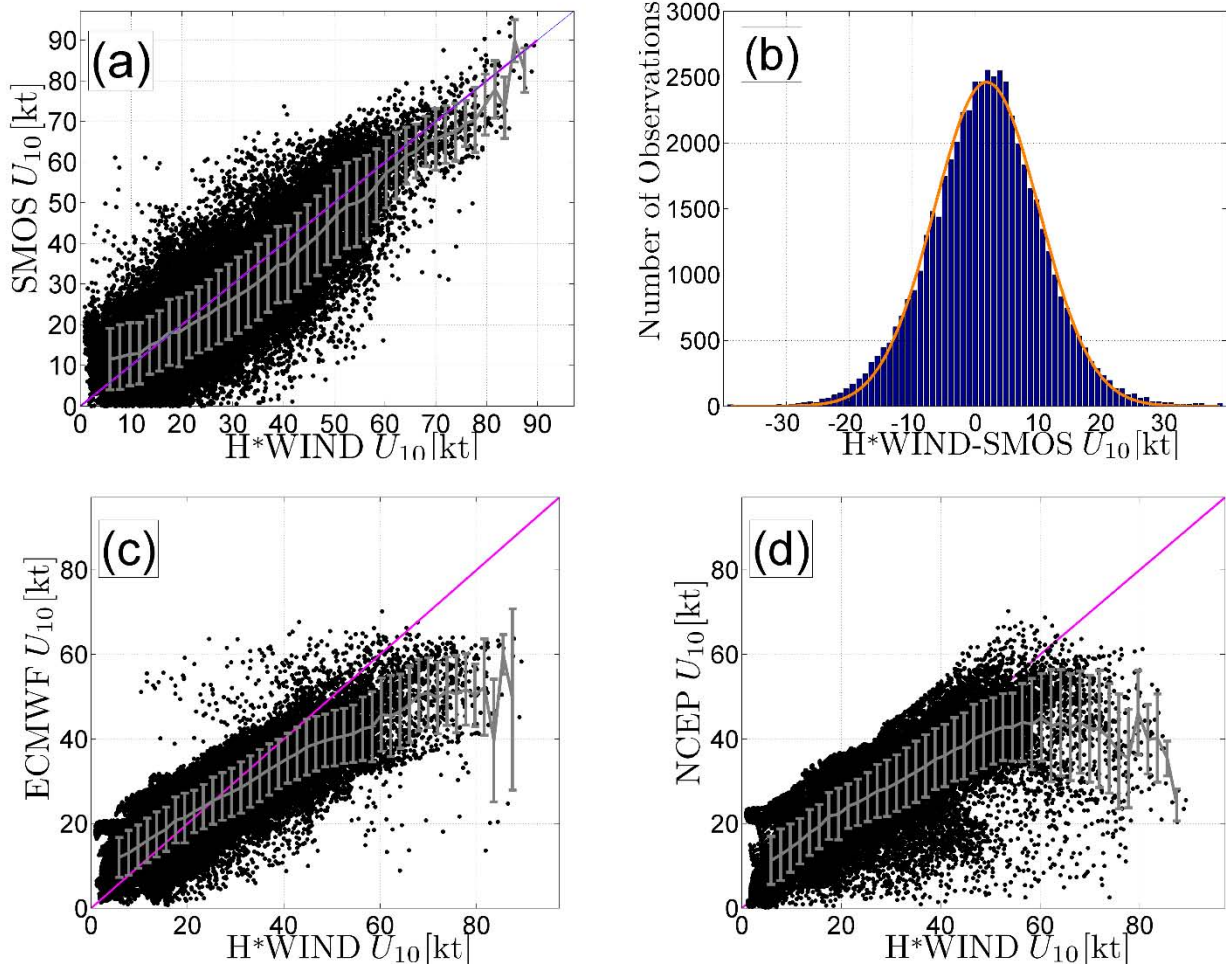
728

729 According to the sensitivity of the GMF (~ 0.15 K/kt below hurricane force and ~ 0.3 K/kt above 64 kt),
730 the rain effect would translate into maximum wind speed retrieval error of ~ 20 kt (~ 10 m/s) for storms
731 below Category 1 and 10 kt (~ 5 m/s) for storms above. In Fig. 12 bottom panel, we show SMOS excess
732 emissivity Δe further classified as function of rain rate intensity in four classes: no rain, light rain (rain
733 rate RR < 5mm/h), moderate rain (5 mm/h < RR < 10 mm/h) and heavy rain (RR > 10 mm/h). No clear
734 stratification of the Δe as function of increasing rain rate is observed in the data up to H*WIND value of
735 ~ 75 kt, with all observations in rainy conditions lying close around the bi-linear GMF. This suggests that
736 precipitation is not directly responsible for the difference of emissivity between the rain-free and rainy
737 conditions but perhaps a problem with the classification of rain-free data. The departure observed in Fig.

738 12 at high winds (> 75 kt) and heavy rain conditions (>10 mm/h) is likely to be an artefact due to the low
739 number of observations in these conditions although more data are required to draw a firm conclusion.
740 Small ice particles are known to exist between the eye wall and outer rain bands of TC. In addition,
741 graupel ice pellets are often collocated with the radius of maximum tangential wind (Houze et al., 1992).
742 Hurricanes are usually glaciated everywhere above the -5°C vertical level and stratiform cloud areas are
743 dominated by snowflakes at these levels (Black and Hallett., 1986). The variation of ice phase cloud
744 characteristics at the top of TC and the contribution of these clouds and ice hydrometeors to the L-band
745 emission might be a plausible source for the observed rain/rain-free differences in $\Delta\epsilon$. Nevertheless, to
746 the authors knowledge no suitable data characterizing the upper atmosphere in terms of ice-phase content
747 is available to estimate that effect.

748 **4.4 Validation of SMOS winds and relative accuracy with ECMWF and NCEP**

749 The SMOS GMF given in Eq. 7 was derived based on an ensemble of 30 H*WIND products, covering
750 about 20 storms in the Atlantic and Gulf of Mexico over several years. Validating the new GMF with the
751 H*WIND data is of little practical value as the H*WIND data are used to derive the GMF. Instead, we
752 assess the performance of SMOS-derived winds using Numerical Weather Prediction (NWP) products
753 and the 30 collected H*WIND fields as the validation dataset. ECMWF and NCEP surface winds have
754 been co-located with the 30 pairs of SMOS-H*WIND data fields. Residual rain or ice effects degrading
755 the quality of the retrievals as discussed in the previous section are ignored, as there is no methodology
756 to correct for these effects. The difference between H*WIND and the SMOS surface wind speed were
757 evaluated using the bilinear GMF function (GMF1) that was quasi-independently derived from the
758 H*WIND dataset used for here validation. SMOS, ECMWF and NCEP surface winds are compared to
759 the reference H*WIND field in Fig. 13. Compared to Reul et al. (2012) this validation approach will
760 provide a more reliable assessment of the relative quality of SMOS wind speed products because it is
761 based on a significantly larger ensemble of data.



762
763

Fig. 13: (a) Comparisons between co-located SMOS retrievals (GMF1) and H*WIND surface winds for an ensemble of ~ 30 tropical storms and hurricanes over the period 2010-2013 (b) Histogram of the differences between co-located SMOS and H*WIND surface winds. The orange curve is a Gaussian fit with standard deviation of 8.3 kt. (c) H*WIND versus ECMWF winds and (d) NCEP winds versus H*WIND. The gray curves are showing the mean y-axis wind speed in bins of 2 kt width of H*WIND surface wind speed data ± 1 standard deviation. Root mean square differences (RMSD) and biases between each products and H*WIND ones are provided in table 1.

771

772

773

Statistics of the differences between these three estimates of the surface wind speed in TCs and H*WIND

774

data are provided in Table 1.

775

776

777

778

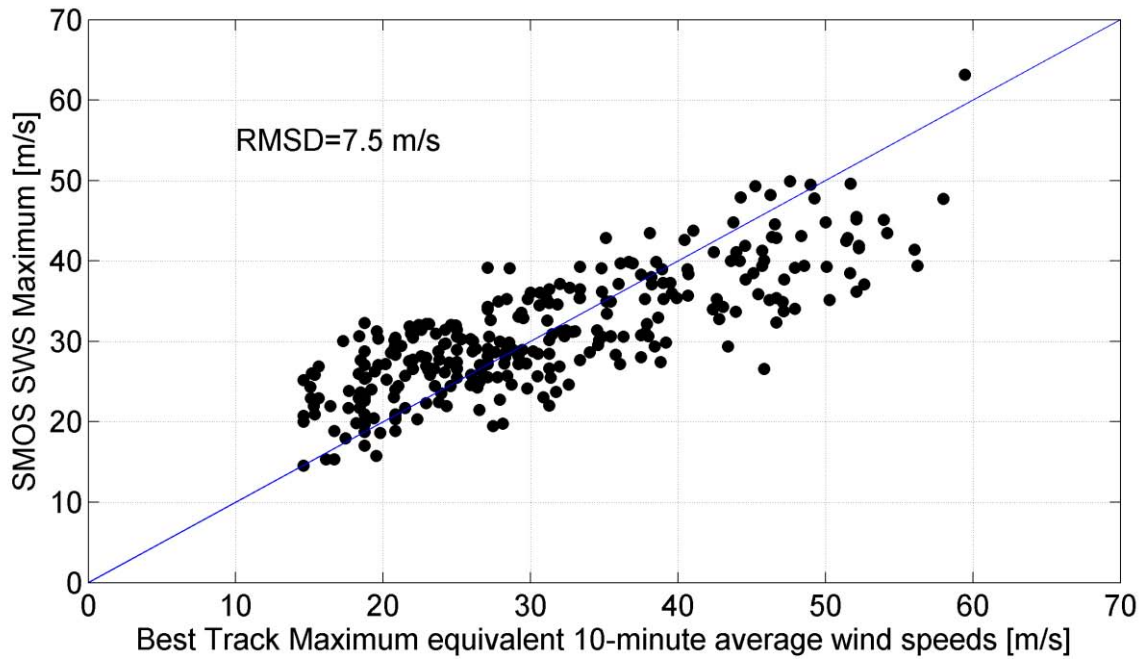
779

780 **Table-1.** Statistics of the differences between co-located H*WIND and SMOS, ECMWF and NCEP
 781 surface wind fields (positive mean difference means that H*WIND is greater than the considered
 782 product).
 783

| | Wind Speed Range (kt) | SMOS | ECMWF | NCEP |
|----------------------|-----------------------|------|-------|------|
| RMSD (kt) | 0-100 | 9.3 | 7.9 | 8.9 |
| Mean difference (kt) | 0-100 | 1.5 | 0.9 | 0.4 |
| RMSD (kt) | 64-100 | 8.1 | 23.5 | 32.4 |
| Mean difference (kt) | 64-100 | 4.3 | 21.6 | 29.2 |

784 As shown in Table-1, the RMS and mean differences between H*WIND products and the three surface
 785 wind speed products are very similar considering the full wind speed range between 0 and 100 kt.
 786 However, above ~64 kt, the SMOS wind speed accuracy outperforms NWP winds with rms and mean
 787 differences between SMOS and H*WIND data of about 8.1 kt and 4.3 kt, respectively whereas both
 788 NCEP and ECMWF products both saturate with increasing wind speed leading to significant biases and
 789 root mean square differences greater than 20 kt in the high wind speed range when compared to
 790 H*WIND.
 791

792 We have shown that the ‘average’ L-band brightness temperature excess is a monotonically increasing
 793 parameter with increasing storm intensity. The highest wind regions often extending over domains of, or
 794 smaller than, 100 km, with very significant wind speed gradients found over small distances relative to
 795 the SMOS spatial resolution, particularly in the eyewall region. Given the relatively low spatial resolution
 796 of the SMOS instrument (~43 km) maximum sustained wind speeds, a key parameter in all
 797 parameterization of hurricane wind field dynamics, are retrieved from SMOS but lacking small-scale
 798 features (this was clearly seen when comparing SMOS wind retrievals with SFMR aircraft measurements).



799
800
801
802

Figure 14: Relationships between the maximum of SMOS winds as function of the Best track Maximum Sustained Wind speed.

803
804
805
806
807
808
809
810
811

To assess the quality of the maximum wind speed inferred from SMOS products, we compared the maximum wind derived from Eq. 7 computed for each of the 300 storms in the SMOS-STORM database to the 6-hourly Best Track maximum wind interpolated to the SMOS acquisition time. The comparison between both estimates is shown in Fig. 14 which shows that the maximum wind derived from SMOS correlates well with the Best-track maximum sustained wind. The RMS difference is nevertheless higher than it was found for all-wind speed comparisons, reaching ~14.5 kt. An underestimation of the maximum wind is also systematically visible in the SMOS products above ~75 kt. The spatial-smoothing effect of the satellite sampling, with a predominant impact in the very high wind and high gradient regions is thought to be the cause of this underestimation.

812 **5 Conclusions and perspectives**

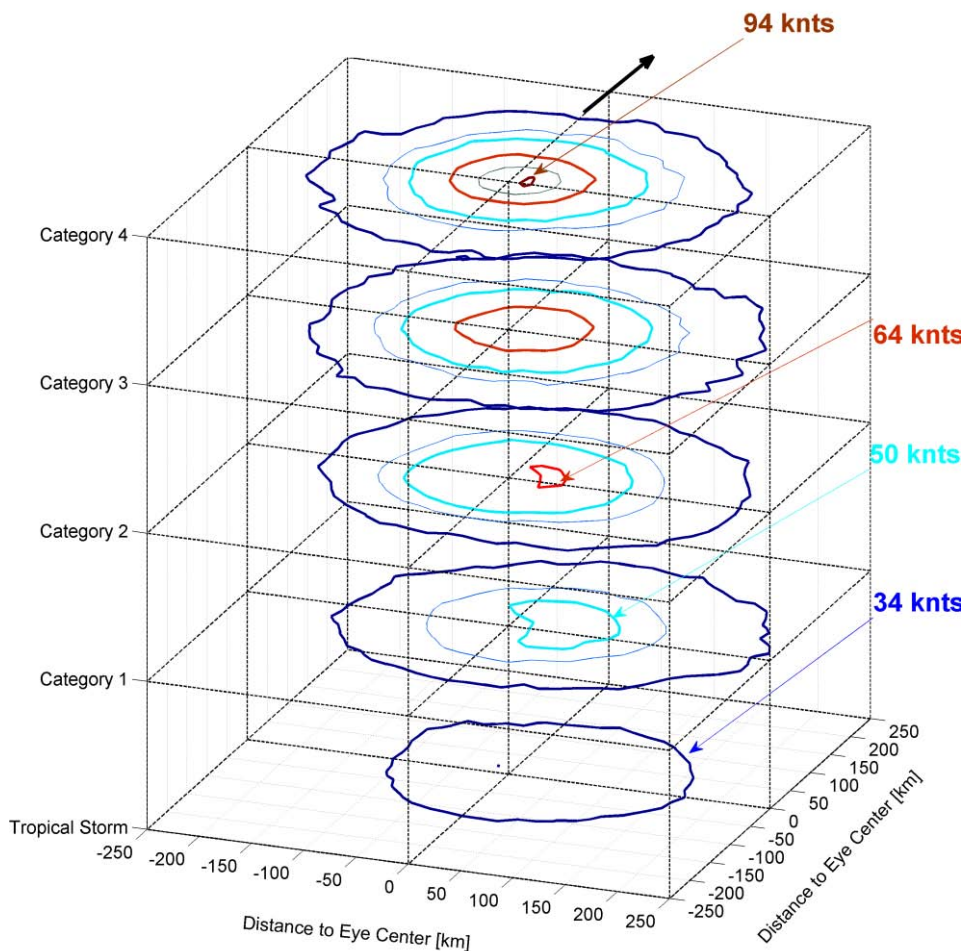
813
814
815
816
817

Five years (May 2010- April 2015) of SMOS L-band brightness temperature data intercepting a large number of Tropical Cyclones at global scale have been analysed in this paper. A subset of about 300 intercepts have been carefully selected to provide the highest quality measurements available covering the full range of storm intensities on the Saffir-Simpson Wind Scale. The storm-induced half-power

818 radio-brightness contrast, ΔI , was estimated for each SMOS intercept with storms and expressed in a
819 common storm-centric coordinate system. The 2D mean and standard deviation of the ΔI were further
820 evaluated for each storm intensity class of the Saffir-Simpson Wind Scale. The average distribution of ΔI
821 I show that the mean brightness contrast amplitude coherently increases with increasing TC intensity.
822 The radii within which the brightest ΔI values are found for each TC category is found to diminish as
823 the storm intensity increases, consistent with the reported evolution of the highest surface wind
824 distribution in TC (Holland, 1980). The mean brightness contrast is monotonically increasing with storm
825 intensities from about 5 K for tropical storms up to ~ 24 K for the most intense category 5 cyclones
826 without showing saturation above hurricane force (64 kt) illustrating the potential of the SMOS data for
827 better monitoring TC intensification. A remarkable feature of the mean ΔI fields is that the maxima of
828 ΔI are systematically found on the right-hand side quadrants of the storms. This is consistent with the
829 reported asymmetric structure of the wind and wave fields in TC conditions: the maximum wind speed
830 and sea surface height generally occur in the right-hand quadrants of storms (in the northern-hemisphere)
831 because of the relative wind and extend-fetch effects created by a translating storm. For category 1-5
832 TCs, the ΔI standard-deviation exhibits a quasi-annular distribution around the storm centre, with local
833 minima at the centre, consistent with the relatively calm eye of a TC. For storm intensities above and
834 including category 4 on the Saffir Simpson Wind Scale, the SMOS instrument is not able to resolve the
835 detailed structure of TC eye winds for those most intense storms that have a maximum wind radii below
836 the SMOS pixel size (~ 43 km).

837 A revision of the bi-linear GMF proposed by Reul et al. (2012) has been derived using a much larger
838 ensemble of co-located SMOS, SMFR flight track data and analysed 2D H*Wind fields. We found that
839 the L-band radio-brightness contrast evolves quadratically with surface wind speed and we propose an
840 empirical parametric law relating ΔI and the 10 m height surface wind speed U_{10} . Major differences
841 with the GMF of Reul et al. (2012) are found in the low to moderate wind speed regimes. Use of the new
842 GMF will help reduce observed biases in the SMOS surface wind retrievals below 50 kt.

843 Using co-located rain rate estimates from CMORPH, we shown that the L-band radio-brightness
844 contrasts measured in TC rain-free conditions do not evolve similarly with wind speed compared to those
845 acquired during precipitation events. Differences as large as 3K translate into maximum surface wind
846 speed errors of ~20 kt below hurricane force (~64 kt) and ~10 kt above. Larger errors are found in the
847 lowest wind speed regime because of the smaller sensitivity of the ΔI function to wind speed below
848 hurricane force. However, further classification of these data as function of increasing rain rate for fixed
849 wind speed values did not reveal any significant dependencies with increasing rain rate. This seems to
850 indicate that other geophysical contributions are responsible for the observed differences in ΔI during
851 rain-free and rainy conditions. The variation of ice phase hydrometeor characteristics at the top of
852 cyclones and the associated varying contributions of clouds to the L-band emission might be a plausible
853 source.



854 **Fig. 15.** Synoptic structure of the surface wind field in Tropical Cyclones as retrieved from SMOS data
855 as function of the Saffir-Simpson High Wind intensity scale. Average 2D wind fields from SMOS are
856

857 contoured at levels of 34 (thick dark blue), 44 (thin blue), 50 (thick cyan), 64 (thick red), 80 (gray) and
858 94 (thick chesnut) kt. The thick black arrow is indicating the averaged storm propagation direction.

859
860
861 Neglecting the potential rain/ice impacts, we compared SMOS, ECMWF and NCEP winds to a large
862 ensemble of H*WIND 2D fields spatially averaged at the SMOS ~43 km nominal spatial resolution.
863 Using the GMF of Reul et al. (2012), results showed that the surface wind speed in TCs can be retrieved
864 from SMOS data with an RMS error on the order of 8-9 kt up to 100 kt. Better performance is expected
865 with a new quadratic GMF. SMOS wind product performances when compared to H*WIND ‘ground-
866 truth’ data in the hurricane wind speed range (above 64 kt) are found to be a factor 3 to 4 better than the
867 those from the NWP products: NWP fields significantly underestimating the surface wind speed in
868 extreme conditions. The maximum wind speed estimated from SMOS was shown to be consistent with
869 best-track wind analysis estimates with an RMS error of ~14 kts. This degraded accuracy for the wind
870 maxima is thought to be caused by 1) the spatial-smoothing effect of the SMOS instrument sampling in
871 the high-wind gradient zones of the eyewalls and 2) a potentially higher effect of cloud ice and cloud on
872 the L-band emissivity in these regions.

873 Applying the new quadratic GMF function to the average radio-brightness contrasts estimated as
874 function of storm intensities, we are now in a position to provide a synoptic view of the surface wind
875 field observed by an L-band passive sensor in tropical cyclones. This allows us to study TC structural
876 evolution as function of increasing TC intensities as shown in Fig 15. As the storm intensity increases,
877 the wind speed above a certain threshold spreads within a quasi-circular domain of almost constant radii:
878 ~200 km for winds above 34 kt, 120 km for winds above 50 kt and ~75 km for winds above 64 kts.
879 Following the approach of Chavas et al., (2015) who used historical datasets of QuickSCAT satellite
880 scatterometer observations to analyse the wind structures in the outer region of tropical cyclones at large
881 radii, the SMOS synoptic wind structure could be used to assess the quality of available Hurricane wind
882 models (e.g. Holland, 1980) for almost the complete radial structure of the low-level tropical cyclone
883 wind field.

884 Average 2D wind fields from SMOS show that the radii of the most intense winds always start to
885 appear on the right-hand (N. Hemisphere) quadrants of the storms for a given intensity. An important
886 result of this study is that the average L-band brightness temperature systematically indicates maxima in
887 the right-hand (N. Hemisphere) quadrants of the storms above hurricane force. This is consistent with
888 reported structures in TC wind models but waves and associated generation of foam are also known to
889 show large asymmetries in storm quadrants with clearly evidenced maxima in significant wave height
890 found in the right-hand (N. Hemisphere) quadrants because of the ‘extended-fetch’ effect (Young, 2003).
891 The relative contributions of wind and waves to the increase of L-band radio-brightness contrasts remain
892 uncertain and need further detailed investigation e.g., using systematic co-localizations between SMOS
893 data, ground-truth surface winds, and wind and sea state measurements from altimeters (Quilfen et al.,
894 2011). A very promising perspective is the creation of a passive low-microwave frequency-based surface
895 wind speed storm catalogue to be built by merging data from SMOS, AMSR2 and SMAP sensors to
896 provide an enhanced storm tracking capability. SMOS data provide a global coverage about every 3 days.
897 However, during fast evolving storm events, SMOS may just capture a portion of the storm or miss it
898 entirely. In addition, SMOS data can be heavily contaminated in some areas by RFI, solar effects or land
899 contamination. RFI are particularly problematic in the North west Pacific and in the Bay of Bengal.
900 Combining SMOS, SMAP and AMSR2 retrievals will definitively help better characterizing high wind
901 speed and storm events over the globe. These are on-going efforts within the European Space Agency
902 (ESA) SMOS-STORM project.

903 With the recent development of new methodologies to retrieve surface wind speed in all weather
904 conditions from X, C and L-band radiometer measurements from Space (Meissner and Wentz, 2009; El-
905 Nimri et al., 2010, Reul et al., 2012, Zabolotskikh, 2015) the synergy of passive microwave observations
906 from space operating in the X to L-bands (AMSR2, WindSat, SMOS and SMAP) can now be envisaged.
907 The complementarity and added-value to scatterometer data (eg. ASCAT and RapidSCAT) and NWP
908 products (ECMWF and NCEP) is obvious and will be studied in more detail in the frame of our on-going
909 study. Ultimately we aim to produce new blended surface wind speed products from all products

910 including the SMOS high wind speed data building on the new methodology currently developed by
911 Zabolotskikh et al. (2015). For SMAP, a similar algorithm than the one presented in this paper for SMOS
912 can be applied.

913 On-going efforts are also in progress to demonstrate the utility, performance and impact of SMOS-
914 STORM products on TC and extratropical storm prediction systems in the context of maritime
915 applications. Comparisons of the SMOS wind speed data with short range forecasts of 10m winds from
916 the Met Office global model background are now performed to generate observed minus background
917 values (O-B). The impact of assimilating SMOS wind speeds will be demonstrated by diagnosing
918 changes to the mean global atmospheric analyses e.g. low-level wind field, pressure at mean sea level
919 (PMSL), etc. Comparing various forecast variables (e.g. wind, surface pressure, geopotential height) with
920 quality-controlled observations valid at the same time/location and calculating the difference in root
921 mean square (RMS) error between the trial and control values will be conducted to show how changes
922 in the analysis as a result of assimilating SMOS wind speed observations affect global model forecasts
923 (so-called global NWP index).

924 **6 ACKNOWLEDGEMENTS**

925

926 We would like to acknowledge the support of ESA Support to Science Element program under the
927 contract SMOS+STORM evolution, #4000105171/12/I-BG.

928

929 **7 REFERENCES**

930

943 Anguelova, M.D.; Gaiser, P.W. Dielectric and Radiative Properties of Sea Foam at Microwave
944 Frequencies: Conceptual Understanding of Foam Emissivity. *Remote Sens.* **2012**, *4*, 1162-1189.

945

946 Anterrieu, E., P. Waldteufel, and A. Lannes (2002), Apodization functions for 2-D hexagonally sampled
947 synthetic aperture imaging radiometers, *IEEE Trans. Geosci. Remote Sens.*, 40(12), 2531–2542,
948 doi:10.1109/TGRS.2002.1176146

949

950

951 Black, R.A., and J. Hallett (1986), Observations of the distribution of ice in hurricanes" *J. Atmos. Sci.*,
952 43, pp.802-822

953

954 Brinkman, S., and Bodschwinn, H. (2003). Advanced gaussian filters. *Advanced techniques for*
955 *assessment surface topography*. Kogan Page, London, 63-91.

956

957 Camps, A., et al. (2005), The emissivity of foam-covered water surface at L-band: Theoretical modeling
958 and experimental results from the FROG 2003 field experiment, *IEEE Trans. Geosci. Remote Sens.*, 43,
959 925–937, doi:10.1109/TGRS.2004.839651

960

961 Chavas, D. R, N. Lin, and K. A. Emanuel (2015), A model for the complete radial structure of the
962 tropical cyclone wind field. Part I: Comparison with observed structure, *Journal of the Atmospheric*
963 *Sciences*, doi: <http://dx.doi.org/10.1175/JAS-D-15-0014.1>

964

965 Donlon, C. J., M. Martin, J. D. Stark, J. Roberts-Jones, E. Fiedler and W. Wimmer, (2012), The
966 Operational Sea Surface Temperature and Sea Ice analysis (OSTIA), *Remote Sensing of the*
967 *Environment*, 116, 140-158, doi: 10.1016/j.rse.2010.10.017 2011.

968

969 Donnelly, W. J., J. R. Carswell, R. E. McIntosh, P. S. Chang, J. Wilkerson, F. Marks, and P. G. Black
970 (1999), Revised ocean backscatter models at C and Ku band under high-wind conditions, *J. Geophys.*
971 *Res.*, 104(C5), 11485–11497, doi:[10.1029/1998JC900030](http://dx.doi.org/10.1029/1998JC900030).

972

973 El-Nimri, S. F., W. Lindwood Jones, E. Uhlhorn, C. Ruf, J. Johnson, and P. Black (2010), An improved
974 C-band ocean surface emissivity model at hurricane-force wind speeds over a wide range of Earth
975 incidence angles, *IEEE Geosci. Remote Sens. Lett.*, 7, 641–645, doi:10.1109/LGRS.2010.2043814.

976

977 Entekhabi, D., S. Yueh, P. O'Neill, K. Kellogg et al., *SMAP Handbook*, JPL Publication JPL 400-1567,
978 Jet Propulsion Laboratory, Pasadena, California, 182 pages, 2014. - See more at:
979 <https://www.cuahsi.org/Posts/Entry/11508#sthash.K9plxnN0.dpuf>

980

981 Golbraikha E. and Y. M. Shtemler, Foam input into the drag coefficient in hurricane conditions,
982 *Dynamics of Atmospheres and Oceans*, Vol 73, pp 1–9, 2016, ISSN 0377-0265,
983 <http://dx.doi.org/10.1016/j.dynatmoce.2015.10.005>..

984

984 Holthuijsen, L. H., M. D. Powell, and J. D. Pietrzak (2012), Wind and waves in extreme hurricanes, *J.*
985 *Geophys. Res.*, 117, C09003, doi:[10.1029/2012JC007983](http://dx.doi.org/10.1029/2012JC007983).

986

986 Holland G. J., 1980: An Analytic Model of the Wind and Pressure Profiles in Hurricanes. *Mon. Wea.*
987 *Rev.*, **108**, 1212–1218. doi: [http://dx.doi.org/10.1175/1520-0493\(1980\)108<1212:AAMOTW>2.0.CO;2](http://dx.doi.org/10.1175/1520-0493(1980)108<1212:AAMOTW>2.0.CO;2)

988

- 989 Horstmann, J., C. Wackerman, S. Falchetti, and S. Maresca. 2013. Tropical cyclone winds retrieved from
990 synthetic aperture radar. *Oceanography* 26(2):46–57, <http://dx.doi.org/10.5670/oceanog.2013.30>.
- 991 Houze, R. A., Jr., P. V. Hobbs, K. R. Biswas, and W. M. Davis, 1976: Mesoscale rainbands in
992 extratropical cyclones. *Mon. Wea. Rev.*, 104, 868-878.
- 993 Houze, R. A., Jr., F. D. Marks, Jr., and R. A. Black, 1992: Dual-aircraft investigation of the inner core
994 of Hurricane Norbert. Part II: Mesoscale distribution of ice particles. *J. Atmos. Sci.*, 49, 943-962.
- 995 Jarvinen, B. R., C. J. Neumann, and M. A. S. Davis (1984), A tropical cyclone data tape for the North
996 Atlantic Basin, 1886 – 1983: Contents, limitations and uses, Tech. Memo. NWS NHC-22, 21 pp., NOAA,
997 Silver Spring, Md
- 998 Joyce, R. J., J. E. Janowiak, P. A. Arkin, and P. Xie, (2004), CMORPH: A method that produces global
999 precipitation estimates from passive microwave and infrared data at high spatial and temporal resolution..
1000 *J. Hydromet.*, 5, 487-503.
- 1001 Klotz, B. W., and E. W. Uhlhorn, (2014), Improved Stepped Frequency Microwave Radiometer Tropical
1002 Cyclone Surface Winds in Heavy Precipitation. *J. Atmos. Oceanic Technol.*, **31**, 2392–2408.
1003 doi: <http://dx.doi.org/10.1175/JTECH-D-14-00028.1>
- 1004 Knaff, J. A. Mark DeMaria, Debra A. Molenaar, Charles R. Sampson, and Matthew G. Seybold, 2011:
1005 An Automated, Objective, Multiple-Satellite-Platform Tropical Cyclone Surface Wind Analysis. *J. Appl.*
1006 *Meteor. Climatol.*, **50**, 2149–2166. doi: <http://dx.doi.org/10.1175/2011JAMC2673.1>
1007
- 1008 Knapp, K. R., M. C. Kruk, D. H. Levinson, H. J. Diamond, and C. J. Neumann, 2010:
1009 The International Best Track Archive for Climate Stewardship (IBTrACS): Unifying tropical cyclone
1010 best track data. *Bulletin of the American Meteorological Society*, 91, 363-
1011 376. doi:10.1175/2009BAMS2755.1
1012
- 1013 Kudryavtsev, V., P. Golubkin, and B. Chapron (2015), A simplified wave enhancement criterion for
1014 moving extreme events, *J. Geophys. Res. Oceans*, 120, doi:[10.1002/2015JC011284](http://dx.doi.org/10.1002/2015JC011284).
1015
- 1016 MacAfee, A. W., and P. J. Bowyer, 2005: The modeling of trapped-fetch waves with tropical cyclones–
1017 A desktop operational model. *Wea. Forecasting*, **20**, 245–263.
1018
- 1019 Meissner, T., and F. J. Wentz (2009), Wind vector retrievals under rain with passive satellite microwave
1020 radiometers, *IEEE Trans. Geosci. Remote Sens.*, 47, 3065–3083, doi:10.1109/TGRS.2009.2027012
1021
- 1022 Molinari, J., and S. Skubis, 1985: Evolution of the surface wind field in an intensifying tropical
1023 cyclone. *Journal of the Atmospheric Sciences*, **42**, 2865-2879.
1024
- 1025 Norberg, W., J. Conaway, D. B. Ross, and T. Wilheit, Measurements of microwave emission from a
1026 foam-covered, wind-driven sea, *J. Atmos. Sci.*, 429–435, 1971.
1027
- 1028 Newell A.C. and V. E. Zakharov, Rough sea foam, *Phys. Rev. Lett.* **69**, 1149, 1992
1029
- 1030 Powell, M. D., S. H. Houston, L. R. Amat, and N. Morisseau-Leroy (1998), The HRD real-time hurricane
1031 wind analysis system, *J. Wind Eng. Ind. Aerodyn.*, 77–78, 53–64, doi:10.1016/S0167-6105(98)00131-7.
1032

1033 Powell, M.D., 2010: "Near-surface based, airborne, and satellite observations of tropical cyclones." *In*
1034 *Global Perspectives on Tropical Cyclones: From Science to Mitigation*, J.C.L. Chan and J.D. Kepert
1035 (Eds.). World Scientific Publishing Company, 2nd edition, p. 177-199.

1036
1037 Quilfen Yves, Vandemark Doug, Chapron Bertrand, Feng Hui, Sienkiewicz Joe (2011). Estimating Gale
1038 to Hurricane Force Winds Using the Satellite Altimeter. *Journal of Atmospheric and Oceanic*
1039 *Technology*, 28(4), 453-458. <http://dx.doi.org/10.1175/JTECH-D-10-05000.1>

1040
1041
1042 Rogers, R., and E. Uhlhorn (2008), Observations of the structure and evolution of surface and flight-level
1043 wind asymmetries in Hurricane Rita (2005), *Geophys. Res. Lett.*, 35, L22811,
1044 doi:[10.1029/2008GL034774](https://doi.org/10.1029/2008GL034774).

1045
1046 Ruf, C., A. Lyons, M. Unwin, J. Dickinson, R. Rose, D. Rose and M. Vincent, "CYGNSS: Enabling the
1047 Future of Hurricane Prediction," *IEEE Geosci. Remote Sens. Mag.*, **Vol. 1**, No. 2, 52-67, doi:
1048 10.1109/MGRS.2013.2260911, 2013

1049
1050 Reul N. and B.Chapron (2003). A model of sea-foam thickness distribution for passive microwave
1051 remote sensing applications. *Journal of Geophysical Research Oceans*, 108(C10).

1052
1053 Reul & Ifremer CATDS-CECOS Team 2011, SMOS L3 SSS Research products: Product validation &
1054 Product User Manual Documents Reprocessed Year 2010: IFREMER, Plouzané, France

1055
1056 Reul N., Tenerelli J., Chapron B., Vandemark D., Quilfen Y., and Y. Kerr, "SMOS satellite L-band
1057 radiometer: A new capability for ocean surface remote sensing in hurricanes", *Journal of Geophysical*
1058 *Research*, vol. 117, C02006, doi: 10.1029/2011JC007474, (2012).

1059
1060 Ross, D. B., and V. Cardone, Observations of oceanic whitecaps and their relation to remote
1061 measurements of surface wind speed, *J. Geophys. Res.*, **79**, 444–452, 1974.

1062
1063 Skou, N., and D. Hoffman-Bang (2005), L-band radiometers measuring salinity from space: Atmospheric
1064 propagation effects, *IEEE Trans. Geosci. Remote Sens.*, 43, 2210–2217,
1065 doi:10.1109/TGRS.2005.856115.

1066
1067 Uhlhorn, E. W., P. G. Black, J. L. Franklin, M. Goodberlet, J. Carswell, and A. S. Goldstein, 2007:
1068 Hurricane surface wind measurements from an operational stepped frequency microwave radiometer.
1069 *Mon. Wea. Rev.*, 135, 3070-3085.

1070
1071 Uhlhorn, E. W., B. W. Klotz, T. Vukicevic, P. D. Reasor, and R. F. Rogers, 2014: Observed hurricane
1072 wind speed asymmetries and relationships to motion and environmental shear. *Mon. Wea.*
1073 *Rev.*, **142**, 1290–1311, doi:10.1175/MWR-D-13-00249.1.

1074
1075 Webster, W. J., T. T. Wilheit, D. B. Ross, and P. Gloersen, Spectral characteristics of the microwave
1076 emission from a wind-driven foam covered sea, *J. Geophys. Res.*, **81**, 3095–3099, 1976.

1077
1078 Weissman, D.E., Bourassa, M. A. and Tongue, J. (2002) Effects of rain rate and wind magnitude on Sea
1079 Winds scatterometer wind speed errors. *Journal of Atmospheric and. Oceanic Technology*. 19, pp. 738-
1080 746

1081
1082 Willoughby, H.E., and M. B. Chelmon, 1982, "Objective determination of hurricane tracks from aircraft
1083 observations", *Mon. Wea. Rev.*, **110**, p.1298-1305.

1085 Young, I. R. 2003: “A Review of the Sea State Generated by Hurricanes “, Marine Structures. 16, 201-
1086 218
1087
1088 Yueh, S. H., R. West, W. J. Wislon, F.K. Li, E.G. Njoku, and Y. Rahmatsamii (2001), Error sources and
1089 feasibility for microwave remote sensing of ocean surface salinity, IEEE Trans. Geosci. Remote Sens.,
1090 39, 1049–1060, doi:10.1109/36.921423.
1091
1092 Yueh, S. H., S. J. Dinardo, A. G. Fore, and F. K. Li (2010), Passive and active L-band microwave
1093 observations and modeling of ocean surface winds, IEEE Trans. Geosci. Remote Sens., 48(8), 3087–
1094 3100, doi:10.1109/TGRS.2010.2045002.
1095
1096 Zine S, Boutin J, Font J, Reul Nicolas, Waldteufel P, Gabarro C, Tenerelli Joseph, Petitcolin F, Vergely
1097 J, Talone M, Delwart S (2008). Overview of the SMOS sea surface salinity prototype processor. *IEEE-*
1098 *Transactions on geoscience and remote sensing*, 46(3), 621-645.
1099
1100 Zabolotskikh E., Mitnik L. M., Reul N. and B. Chapron (2015). New Possibilities for Geophysical
1101 Parameter Retrievals Opened by GCOM-W1 AMSR2. *IEEE Journal of Selected Topics in Applied Earth*
1102 *Observations and Remote Sensing*, PP(99), 1-14. Publisher's official version :
1103 <http://dx.doi.org/10.1109/JSTARS.2015.241651>.
1104
1105
1106
1107
1108
1109
1110
1111
1112
1113
1114
1115
1116
1117
1118
1119
1120
1121
1122
1123
1124
1125
1126
1127
1128
1129
1130
1131
1132
1133
1134
1135
1136
1137
1138
1139

List of Figure Captions

Fig. 1. Contours of storm-surface induced brightness temperature contrasts ΔI [K] estimated from SMOS L-band data for an ensemble of storms in the Eastern Tropical Pacific (a), Southern Indian Ocean (b), North Atlantic (c), and Western Pacific ocean (d) during 2010-2015. The black thin curves indicate the storm tracks. The coloured contours indicate the amplitude of the storm-induced radio-brightness temperature contrasts [K].

Fig. 2: Examples of SMOS L-band radio-brightness temperature contrasts ΔI [K] measured for tropical Storms (a,b,c: $35 \leq U_{10} \leq 63$ kts), category 1 TC (d,e,f: $64 \leq U_{10} \leq 82$ kts), category 2 TCs (g,h,i: $83 \leq U_{10} \leq 95$ kts), category 3 TCs (j,k,l: $96 \leq U_{10} \leq 113$ kts) and category 4 TCs (m,n,o: $114 \leq U_{10} \leq 135$ kts) on the SSWS. Note that the color-scale range is 0-12 K for TS and category 1, 0-15 K for category 2 to 3 and 0-18 K for category 4 on the SSWS. Each panel represent a domain of about 1000 km width centred on the TC eye. The pink dotted curves show the storm 6-hourly best track and the black arrow indicate the storm main propagation direction but not its motion speed.

Fig. 3: (a): SMOS ΔI estimated over Category 3 TC Jova at 12:32 Z on 10 October 2011. The pink dotted curve shows the Best Track of Jova; the white filled dot and squares indicate the eye location estimated by linear interpolation of the Best Track data at SMOS acquisition time and from the closest 85 GHz acquisitions. In this case, the latter is obtained from SSMIS/17 imagery at 12:59 Z (b). (c) and (d) panels: same fields as top panels but provided in a storm-centric frame of 1000 km² and rotated with respect the storm heading “North Up” that is shown as a white arrow.

Fig. 4. Storm centric contours of the mean (left panels) and standard deviation (right panels) of the L-band radio brightness half power contrast (ΔI [K]) as function of storm sector and intensity. The wind intensity is ranging from tropical storms (top panels, $35 \leq U_{10} \leq 63$ kts), Category 1 TCs (second panels from top, $64 \leq U_{10} \leq 82$ kts), Category 2 TCs (3rd panels from top, $83 \leq U_{10} \leq 95$ kts), Category 3 TCs (4th panels from top, $96 \leq U_{10} \leq 113$ kts), Category 4 TCs (5th panels from top, $114 \leq U_{10} \leq 135$ kts) and Category 5 (bottom panels, $U_{10} > 135$ kts). Contours range from 1 to 28 K in steps of 0.5 K for the mean and from 0 to 10 K in steps of 0.2 K for the standard deviation. Note that the colour scale range is changing from top to bottom panels.

Fig. 5. Mean radial distribution of the storm-induced L-band half-power radio-brightness contrasts (ΔI [K]) as function of storm intensities (colors) given by the Saffir Simpson wind Scale (a) from the South East to the North West storm quadrants and (b) from the South West to the North East storm quadrants.

Fig. 6. (a) Ensemble of SFMR tracks and associated Wind Speed [knots] used for SMOS-SFMR comparisons, and (b) SMOS L-band excess emissivity ($\Delta \epsilon$) contrasts co-located with SFMR flights.

Fig. 7. (a,c,e,g) superimposed SMOS retrieved wind speed using the GMF of Reul et al (2012, color in knots) and SFMR track (black thick curves) for hurricane Daniele the 28 August 2010 (a), hurricane Karl on 16 September 2010 (c); hurricane Earl on 31 August 2010 (e) and hurricane Rina on 25 Oct 2011. The thin dotted curves indicate the storm tracks. b,d,f,h: corresponding time series of the SFMR retrieved wind speed in m/s (black curve) and rain rate in mm/h (grey curve) at nominal resolution along aircraft track (~3 km). The SFMR retrieved wind speed has been spatially averaged with a running window of 43 km width along track (corresponding to the mean resolution of SMOS interferometer pixels) is shown in blue. The retrieved wind speed from SMOS is shown in red using GMF1 and in magenta using GMF2. The x-axis shows the time lag between SFMR acquisitions and SMOS ones.

Fig. 8: SMOS storm-induced excess L-band emissivity, $\Delta \epsilon$, as function of co-located SFMR wind speed for an ensemble of 64 SMFR flights in the Gulf of Mexico and western Atlantic ocean. The time lags between both observations never exceed 6 h. The red line indicate the first bi-linear GMF proposed in Reul et al. (2012). The cyan curve indicates the mean wind-excess emissivity per 10 kt-width bins and the vertical bars indicate ± 1 standard deviation of the emissivity within each bin.

1194 **Fig. 9.** (a) Surface wind speed retrieved from SMOS (GMF of Reul et al (2012)) in a storm centric
1195 coordinate system for hurricane Leslie on 7th September 2012 at 22:19. (b) H*WIND fields interpolated
1196 at SMOS acquisition time and spatially averaged at 43 km resolution. (c) Mean radial distribution of the
1197 SMOS (black) and H*WIND (blue) surface wind speed from the SW to the NE storm quadrants, and (d)
1198 from the NW to the SE storm quadrants. (e) CMORPH rain rate at SMOS acquisition time. (f) SMOS
1199 retrieved wind speed as function of H*WIND with color indicating the rain rate from CMORPH.

1200
1201 **Fig. 10.** Same caption as Fig.9 except for the case of hurricane Katia on the 6th September 2011 at 09:35 Z.

1202
1203 **Fig. 11:** Wind Excess emissivity Δe as function of co-located H*WIND wind speed for an ensemble of
1204 storms in between 2010 and 2013. The red curve illustrates the SMOS GMF of Reul et al (2012). The
1205 cyan curve show the new 'average' GMF function derived in this paper based on the SMOS and H*WIND
1206 paired data. Δe data have been averaged into bins of H*WIND winds at 5 knots intervals with the vertical
1207 error bar indicating ± 1 standard deviation of the Δe within each wind speed bin.

1208
1209 **Fig. 12:** Potential effects of rain on the excess L-band emissivity Δe in storm conditions. Top: GMF
1210 deduced from the SMOS and H*WIND matchups with rain rate provided from CMORPH=0 (red) and
1211 rain rate > 0 (blue). Bottom: similar caption than for the top plot except that the data are now classified
1212 by ranges of rain rate (RR): RR=0 (red), $0 < RR \leq 5$ mm/h (green), $5 \text{ mm/h} < RR \leq 10$ mm/h (cyan) and
1213 $RR > 10$ mm/h. (blue).

1214
1215 **Fig. 13:** (a) Comparisons between co-located SMOS retrievals (GMF1) and H*WIND surface winds for
1216 an ensemble of ~30 tropical storms and hurricanes over the period 2010-2013 (b) Histogram of the
1217 differences between co-located SMOS and H*WIND surface winds. The orange curve is a Gaussian fit
1218 with standard deviation of 8.3 kt. (c) H*WIND versus ECMWF winds and (d) NCEP winds versus
1219 H*WIND. The gray curves are showing the mean y-axis wind speed in bins of 2 kt width of H*WIND
1220 surface wind speed data ± 1 standard deviation. Root mean square differences (RMSD) and biases
1221 between each products and H*WIND ones are provided in table 1.

1222
1223 **Fig 14:** Relationships between the maximum of SMOS winds as function of the Best track Maximum
1224 Sustained Wind speed.

1225
1226 **Fig. 15.** Synoptic structure of the surface wind field in Tropical Cyclones as retrieved from SMOS data
1227 as function of the Saffir-Simpson High Wind intensity scale. Average 2D wind fields from SMOS are
1228 contoured at levels of 34 (thick dark blue), 44 (thin blue), 50 (thick cyan), 64 (thick red), 80 (gray) and
1229 94 (thick chesnut) kt. The thick black arrow is indicating the averaged storm propagation direction.